UNIVERSITY OF OSLO
Department of Geosciences

Sea Surface Wave Height Estimation from Dual-Sensor Towed Streamer

OKWUDILI CHUKS ORJI

27.08.2012

Series of dissertations submitted to the
Faculty of Mathematics and Natural Sciences, University of Oslo
No. 1274

ISSN 1501-7710

Cover: Inger Sandved Anfinsen.
Printed in Norway: AIT Oslo AS.

Produced in co-operation with Akademika publishing.
The thesis is produced by Akademika publishing merely in connection with the thesis defence. Kindly direct all inquiries regarding the thesis to the copyright holder or the unit which grants the doctorate.

Preface

This thesis has been submitted to the Faculty of Mathematics and Natural Sciences at the University of Oslo in partial fulfillment of the requirements for the degree *Philosophiae Doctor (Ph.D.)*. The work was carried out as collaboration between the department of Geosciences of University of Oslo (UiO) and G&E department of Petroleum GeoServices (PGS) Oslo and funded by The Research Council of Norway through the Industrial Ph.D. project 200362. This work has been supervised by Dr. Walter Söllner (PGS) and Professor Leiv-Jacob Gelius (UiO).

Acknowledgement

I thank Almighty God the omniscient, omnipotent and omnipresent.

I am immensely grateful to my supervisors Dr. Walter Söllner and Professor Leiv-Jacob Gelius who have guided me patiently, wisely and always have the time and are happy to discuss with me.

I thank my colleagues at PGS especially the G & E department. I will not forget my mate and friend Endrias G. Asgedom.

I am indebted to my family (Nigeria and Norway) whose shoulders have brought me this far.

I express my gratitude to The Norwegian Research Council for funding this project.

Abstract

This thesis addresses the problem of how to image the time-varying sea surface based on dual sensor marine seismic data. Although flat and stationary sea surface assumptions may suffice during the processing of marine seismic data acquired under calm weather conditions, this idealistic sea surface condition is seldom encountered in practice. Thus, such assumptions may lead to miss-interpretation and miss-location of events. In this work a sea surface imaging tool based on dual-sensor data has been developed. These data are decomposed into upgoing and downgoing wavefields and extrapolated to the sea surface where an adequate imaging condition is applied in order to obtain the sea surface image. Time varying changes of the sea surface is obtained by applying the imaging technique in a sliding window. The imaging tool was tested employing scattered data computed from the Helmholtz-Kirchhoff integral with time varying boundaries (representing realistic time-varying sea conditions using the Pierson-Moskowitz spectrum with directivity included). Thus we could model marine seismic experiments efficiently including such effects as streamer depth variation and moving receivers. In the case of a 3D data acquisition set-up, the effect of sparse streamer spacing was shown to give a reduced resolution but with the low-frequency characteristics of the sea surface still preserved. Spectral analyses of the imaged sea surfaces were also carried out and feasible speeds and directions of the moving sea surfaces were recovered. Finally, the technique was applied to field data (both 2D and 3D) acquired from different locations under different sea surface conditions. Realistic sea surface variations both with respect to wave heights, prevailing wind directions and speeds were obtained demonstrating the potential of the proposed technique.

List of Publications

This thesis is based on the following three papers, referred to in the thesis with the Roman numerals: I-III.

I

Orji O. C., W. Söllner and L-J. Gelius, 2010, Imaging the sea surface using dual-sensor towed streamer: Geophysics **75**, P. V111 – V1118.

II

Orji O. C., W. Söllner and L-J. Gelius, 2012, Effects of time-varying sea surface in marine seismic data: Geophysics **77**, P33-P43.

III

Orji O. C., W. Söllner and L-J. Gelius, 2012, 2D time-varying sea surface imaging using 3D towed dual-sensor streamers: Geophysics (Revised version submitted July 2012)

Related Publications

1. Orji O. C., W. Söllner and L-J. Gelius, 2009, Imaging the sea surface using a dual-sensor towed streamer: SEG Expanded Abstracts 28, 2879-2883.

2. Orji O. C., W. Söllner and L-J. Gelius, 2011, Imaging time varying sea surface using dual sensor towed streamer: SEG Expanded Abstracts 30, 3388-3392.

3. Orji, O., W. Söllner, and L. J. Gelius, 2012, Time-varying sea surfaces from 3D dual-sensor streamer data: 74th EAGE conference, Copenhagen, Denmark, Extended Abstracts, A034.

Related Patents

PGS-11-44US

Methods and Systems for Correction of Streamer-Depth Bias in Marine Seismic Surveys

PGS-11-51US

Methods and Systems for Reconstruction of Low Frequency Particle Velocity Wavefield and Deghosting of Seismic Streamer Data

Contents

Chapter 1

Introduction

A seismic survey represents the most important geophysical prospecting method employed to image subterranean formations. The recorded reflection data consist of a large ensemble of time series or seismic traces. The amplitudes of these signals are proportional to the pressure or particle velocity wavefields measured at the locations of the receivers. Controlled artificial sources are usually used to generate the seismic waves. On land, the source comprises of either explosions from dynamites or vibrations from trucks, and the receivers are geophones planted in the ground. On the other hand, a marine seismic data acquisition is carried out using seismic vessels that tow one or several streamers containing hydrophones (and possible particle velocity sensors) as well as marine seismic sources (e.g., air-guns which essentially release highly compressed air bubbles into the water) at "conveniently" chosen depths. A seafloor type of seismic acquisition system involves planting receiver nodes (consisting of geophones and hydrophones) on the ocean floor and recording seismic activities passively (no artificial sources) or actively (employing artificial sources). Nowadays, streamers containing a combination of hydrophones and vectorized sensor(s) are becoming more of an industry standard with PGS being the pioneering company. Figure 1 depicts a schematic of a marine seismic data acquisition set-up.

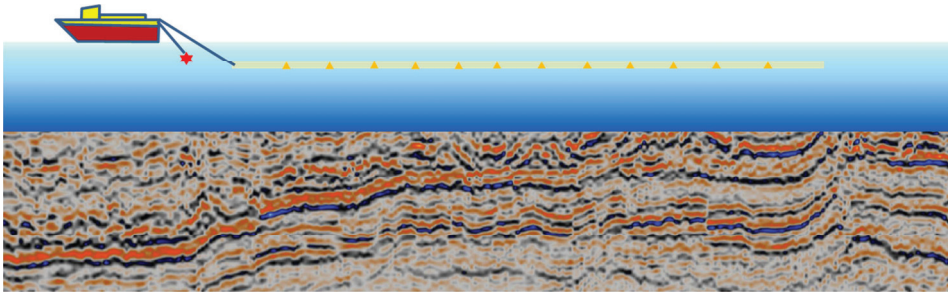

Figure 1: *A cartoon depicting a vessel towing a source (red star) and a line of sensors (yellow triangles) or a streamer at fixed depth within the water layer overlying the earth's geology (subsurface).*

1.1 Marine seismic ghosts

The marine seismic source arrays and steamers are towed at "conveniently" chosen depths fundamentally because excess pressure cannot be measured at free surface (air-water interface) and practically because air-water interface is swamped with noise generated by sea waves. In a calm sea condition, sea surface acts like a mirror. Thus, a time-delayed reflection (also known as ghost) of the source wavefield trails the seismic wavefield travelling directly into the subsurface (primary pulse) from the source location. This means that the effective source signal includes not only the primary pulse but also its ghost. The net effect is that notches are introduced in the amplitude spectrum of the source signal. These notches attenuate certain frequencies depending on the source depth. If the source is towed deep, higher frequencies are attenuated and if it is towed at a shallower depth lower frequencies are attenuated (Ghosh, 2000). The same effect is replicated on the receiver side. It then follows that ghosts reduce seismic resolution. In Figure 2a, the receiver records a total wavefield comprising of the primary pulse (green ray path), source side ghost (red ray path), receiver side ghost (blue ray path) and combined source side and receiver side ghosts (purple ray path). Figure 2b shows plots of the amplitude spectra of source and receiver (hydrophone) sides' ghosts.

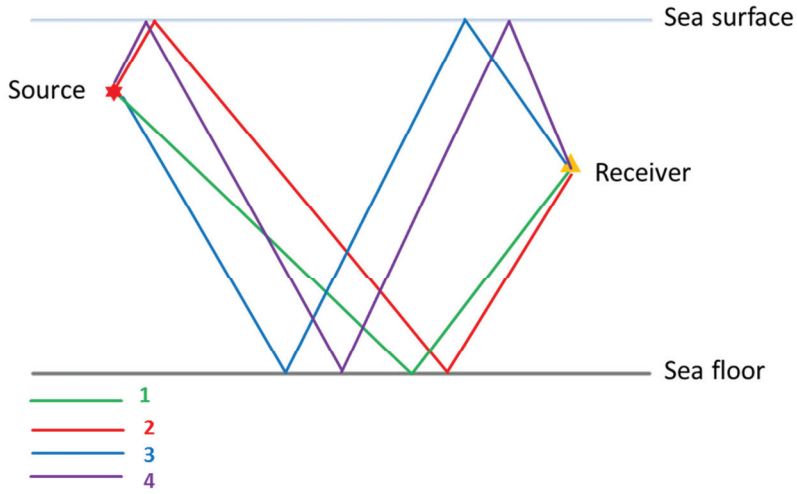

Figure 2a: *A cartoon showing the ray path followed by primary wavefield (green line or ray path 1), source side ghost (red line or ray path 2), receiver side ghost (blue line or ray path 3) and the combined source side and receiver side ghosts (purple line or ray path 4) . The green ray path is the ideal path desired in a marine seismic data acquisition.*

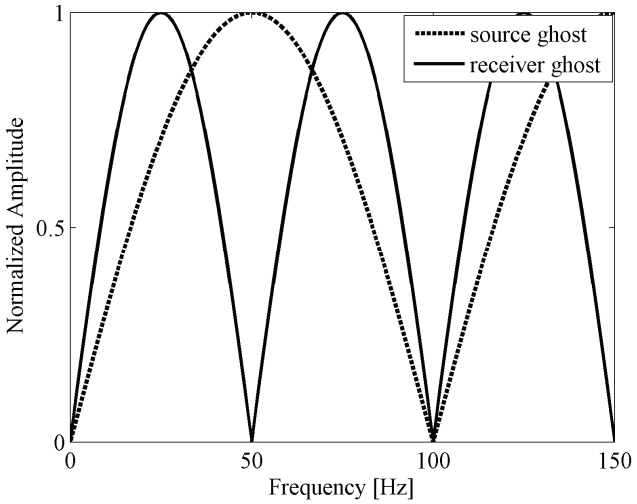

Figure 2b: *Plots showing ghost amplitude spectra of a source placed at 7.5 m and a hydrophone sensor placed at 15 m.*

A high-resolution seismic image of the subsurface is essential for quantitative interpretation and improved reservoir characterization and monitoring. Therefore, the overall goal of the marine seismic industry is to recover the true reflectivity of the subsurface detached of any noise from data acquisition or errors caused by data processing assumptions. However, traditional deghosting of marine seismic data is not a trivial procedure because of the zeros in the spectrum of the ghost filter (Ghosh, 2000). The actual sea surface profile and the reflection coefficient estimates are important input parameters in case of a rough sea deghosting solution. Alternatively, since the frequencies attenuated by ghost notches are related to the source (or the receiver's) towing depth, this can be exploited in removing the ghosts. For example, on the source side, two air-gun arrays can be towed at two different "conveniently" chosen depths such that their notches occur in a complementary manner (i.e., where one source has notch the other does not, see Ziolkowski, 1971; Posthumus, 1993; Parkes and Hegna, 2011). Similarly, this can be replicated on the receiver side (Posthumus, 1993). The basic challenges of this solution are the flat sea surface assumption and maintaining constant towing depths throughout the data acquisition. The latter is more difficult to accomplish on the receiver side because streamers are pliable.

1.2 Collocated dual-sensors

It is a well-known fact that simultaneous measurements of particle velocity and pressure wavefields can eliminate the receiver side ghost during data processing (Schneider et al., 1964; Claerbout, 1976; Barr and Sanders 1989; Amundsen, 1993; Fokkema and van den Berg, 1993). This is because the ghost notches of a hydrophone (pressure sensor) and a geophone (vertical particle velocity sensor) are complementary to each other if these sensors are collocated during data recording. A limitation of dual-sensor data is that the velocity sensor is sensitive to noise at low frequencies (typically from 0 – 20 Hz). This frequency range can be reconstructed from the pressure field measurements by exploiting the relationship between the pressure and vertical particle velocity wavefields (Amundsen et al., 1995). However, sea surface information is needed in order to properly reconstruct these wavefields. Figure 3 show a time recording (top

left) and corresponding ghost amplitude spectrum (top right) of a hydrophone placed at a depth of 15 m. The lower panels in Figure 3 show the scaled time recording (bottom left) and the corresponding ghost amplitude spectrum (bottom right) of a particle velocity sensor measurement. Observe that the velocity sensor record negative pulses for both the primary and ghost pulses unlike the hydrophone which record positive pulse for the primary and a negative pulse for the ghost. This is because pressure is a scalar quantity whereas particle motion is a vector quantity. In this case, positive $z-$direction is chosen downwards. Since the ghost amplitude spectra of the dual-sensor measurements are complementary to each other, this can be exploited during data processing to eliminate the receiver side ghost.

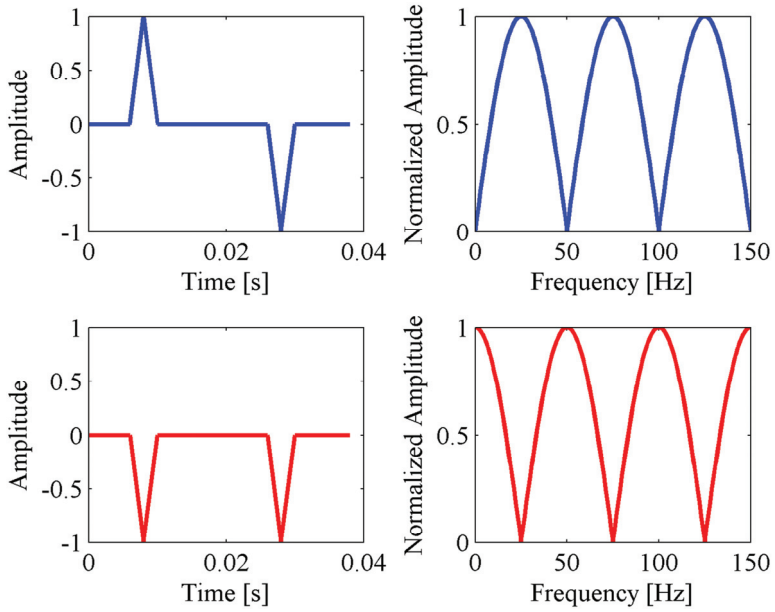

Figure 3: *Time recording of a pressure wavefield (top left) and the corresponding receiver ghost amplitude spectrum (top right). Scaled time recording of a vertical particle velocity sensor (bottom left) and the corresponding receiver ghost amplitude spectrum (bottom right).*

1.3 Low-frequency compensation

The method of using collocated dual sensors to remove the receiver side ghost has one major problem attached: the velocity sensor measurements are swamped by noise (caused by streamer vibrations) at low frequencies. However, at these frequencies velocity data can be reconstructed from hydrophone measurements based on the relationship between the pressure gradient and the vertical particle velocity field. This technique is termed "Low Frequency Compensation (LFC)". The principle behind LFC technique can be explained by considering wavefields $p(x,z,t)$ propagating with speed c in the (x,z) plane of stratified media and satisfying the scalar wave equation:

$$\frac{\partial^2 p}{\partial x^2}+\frac{\partial^2 p}{\partial z^2}=\frac{1}{c^2}\frac{\partial^2 p}{\partial t^2} \tag{1.1}$$

This wave equation can be solved using 2D Fourier transform (space and time) $P(k_x,z,\omega)$ of $p(x,z,t)$:

$$p(x,z,t)=\iint P(k_x,z,\omega)e^{i(k_x x+\omega t)}dk_x d\omega, \tag{1.2}$$

where ω is the angular frequency. The partial derivatives in equation (1.1) are then:

$$\left.\begin{matrix}\frac{\partial^2 p}{\partial x^2}\\ \frac{\partial^2 p}{\partial z^2}\\ \frac{\partial^2 p}{\partial t^2}\end{matrix}\right\}=\iint\left\{\begin{matrix}-k_x^2 P(k_x,z,\omega)\\ \frac{d^2 P(k_x,z,\omega)}{dz^2}\\ -\omega^2 P(k_x,z,\omega)\end{matrix}\right\}e^{i(k_x x+\omega t)}dk_x d\omega \tag{1.3}$$

Thus the wave equation can be transformed into normal differential equation for the Fourier transform $P(k_x, z, \omega)$:

$$\frac{d^2P}{dz^2} + (\frac{\omega^2}{c^2} - k_x^2)P = 0, \tag{1.4}$$

with

$$\frac{\omega^2}{c^2} - k_x^2 = k_z^2$$

The general solution to this differential equation (equation (1.4)) is:

$$P = U + D = Ae^{i(k_z z)} + Be^{i(-k_z z)}, \tag{1.5}$$

where A and B are respectively the amplitudes of the upgoing U and downgoing D wavefields.

Exploiting now the relationship between vertical particle velocity V_z and pressure gradient $\frac{dP}{dz}$ (Berkhout, 1982):

$$V_z = \frac{-1}{i\omega\rho}\frac{dP}{dz}, \tag{1.6}$$

where ρ is the medium density. In case of known pressure measurements P, equation (1.5) can be solved to obtain the general form of the LFC equation (using planewave decomposition):

$$V_z = \frac{k_z}{\omega\rho}\frac{(re^{-ik_z z_R} - e^{ik_z z_R})}{(re^{-ik_z z_R} + e^{ik_z z_R})}P, \tag{1.7}$$

where z_R is the receiver depth, k_z is the vertical wavenumber, r is the reflection coefficient at the water-air interface, $(re^{-ik_z z_R} - e^{ik_z z_R})$ is the velocity sensor ghost function while $(re^{-ik_z z_R} + e^{ik_z z_R})$ is the hydrophone ghost function. Thus, equation (1.7) implies deconvolving the hydrophone ghost from the pressure sensor measurement followed by impedance scaling to convert to velocity sensor measurement and finally convolving with the velocity sensor ghost. A brief derivation of equation (1.7) is given in Section 3.1. Invoking now the special condition of -1 reflection coefficient (i.e., setting r to -1) equation (1.7) gives the simplified version of LFC:

$$V_z = \frac{-k_z}{\omega\rho}\frac{(1+e^{-i2k_z z_R})}{(1-e^{-i2k_z z_R})}P, \tag{1.8}$$

Equation (1.8) is the LFC currently in use because of lack of sea surface information.

1.4 Dual source-arrays

On the source side, assuming that the source pulse is ideal (i.e., emits a spike), a sensor (hydrophone) placed in the vicinity of the source (such that only source side ghost is recorded) records a combined pressure wavefield $s(t)$ comprising of the primary pulse $\delta(t)$ and its ghost $\delta(t-\tau)$ mirrored from the sea surface and separated a time τ from the primary (see Figure 2a). Thus, the measured pressure wavefield $s(t)$ can be represented as a convolution of the primary pulse with a ghost filter $g(t)$ (Ghosh, 2000):

$$s(t) = \delta(t) + r\delta(t-\tau) = \delta(t) * g(t), \tag{1.9}$$

where the symbol * indicates convolution. After planewave decomposition, the emitted wavefield comprises of planewaves of infinite frequencies. If one then considers an arrival with emergence angle $-\theta$ (i.e., incidence angle is θ and specular reflection is assumed on the sea surface) the ghost period τ can then be conceptualized as the time taken for the wavefront to travel from a sensor at depth z_R to the "mirror position" of the sensor situated a distance $-z_R$ above the sea surface as depicted in Figure 4. Thus, the frequency domain representation of the recorded wavefield is:

$$S(\omega) = \Delta(\omega)G(\omega) = \Delta(\omega)(1 + re^{-i\omega\tau}), \tag{1.10}$$

with

$$\tau = \frac{2z_R \cos(\theta)}{c},$$

where c is the speed of sound in water and $G(\omega)$ denotes the spectrum of the ghost filter.

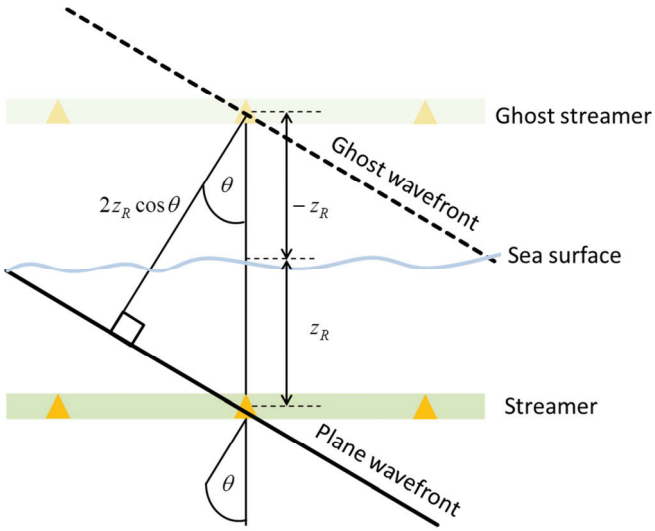

Figure 4: *A cartoon depicting a geometric interpretation of recorded sea surface ghost.*

Assuming the special case of vertical incidence and a reflection coefficient of -1 at the sea surface, the ghost filter can be written as:

$$G(\omega) = (1 - e^{-i\omega\tau}), \qquad \tau = \frac{2z_R}{c} \tag{1.11}$$

The amplitude spectrum is $|G(\omega)| = |2\sin(\omega\tau/2)|$ and suggests periodic notches at the following frequencies:

$$\omega = \frac{k\pi c}{z_R}, \quad k = 0,1,2....., \tag{1.12}$$

It is easily seen that the frequencies at which the notches occur are determined by the source depth. Therefore, by employing two sources placed at different depths such that their ghost notches occur in a complementary manner, the source side ghost can be minimized. The upper panel in Figure 5 shows the ghost amplitude spectra of two sources at depths of 7.5 m and 15 m respectively, whereas the lower panel in the same figure shows the combined amplitude spectrum using the weighted sum method (Posthumus, 1993). One can see that the amplitudes are now recovered at frequencies where the notches of the ghost amplitude spectra of the two sources are complementary. However, the complementarity is not achieved at all frequencies (e.g., at 0 and 100 Hz in this case) and thus, the division by zero at these frequencies introduce large amplitude errors. In addition, the weighted sum method assumes a flat and stationary sea surface. If the sea surface information is available, improved deghosting schemes can be employed.

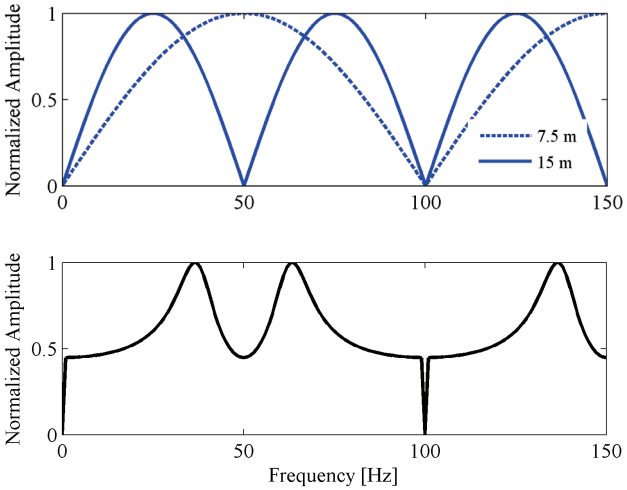

Figure 5: *Plot showing ghost amplitude spectra of two sources placed respectively at 7.5 m and 15 m depths (top panel) and the combined amplitude spectrum (lower panel).*

1.5 Surface related multiples

Most recorded marine seismic data suffer from the occurrence of water-layer multiples. These are multiple reflections trapped between the sea surface (acting as a mirror) and the seafloor. In case of a hard seafloor and shallow water, many orders of multiples are recorded. These multiples can obscure primary reflections from deeper targets and thus penalize seismic interpretation. They are usually predicted based on their relationship with the primary reflections and thus, eliminated. This prediction relies on source and receiver deghosted data. However, flat and stationary sea surface assumptions are made in predicting the multiples. Since sea surfaces vary spatiotemporally, these predictions are not accurate and may introduce errors in the processed data. This is more severe in time-lapse seismic data where changes in sea surface (if not accounted for) might mimic the expected differences in the oil reservoir. Thus, surface

related multiples can be correctly modeled and subsequently removed only if the time-variant sea surface elevation and reflectivity information are available.

Figure 6 is an illustration of a primary reflection (green line), first multiple reflection (dashed green line) and second multiple reflection (dotted green line). In the sketch, other ray paths (e.g., source side ghost) have been ignored for clarity. As one can see, the multiple reflections bounce/reflect from different sea surface heights. The first and the second multiples are 180° out of phase because the first multiple bounced only once from the sea surface on its way to the receiver. This relationship coupled with knowledge of the water depth and the sea surface elevation information can be used to more accurately eliminate the multiples during data processing.

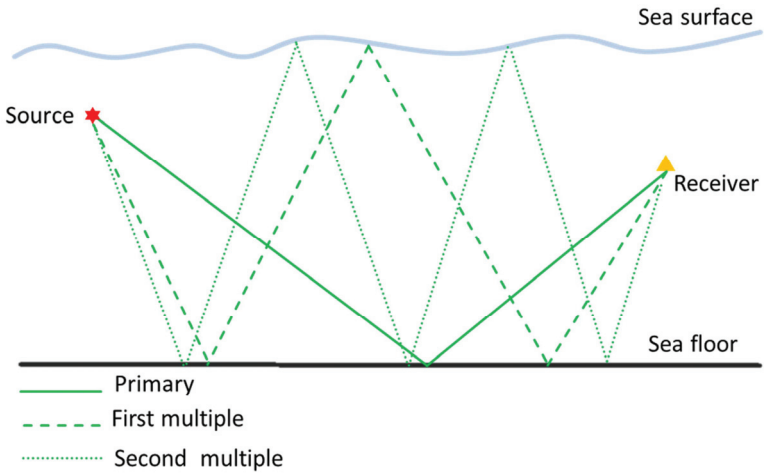

Figure 6: *A sketch showing primary event (green line), its first multiple event (dashed green line) and the second multiple event (dotted green line).*

1.6 Static corrections

Current procedures in marine seismic data processing require a minimal understanding of static corrections. If high fidelity seismic data are to be obtained, variations in the depth elevation of each streamer relative to the assumed reference depth level must be adjusted. During data acquisition and processing, field geometries must be faithfully communicated to the data processing system. Static corrections can then be easily employed in converting actual recording levels to the assumed recording datum (i.e., nominal streamer depth assumed during survey planning). Static corrections are corrections applied to seismic data in order to compensate for effects of streamer and source depth variations relative to the reference or datum (e.g., Sheriff, 1991). In marine seismic data acquisition, time-varying rough sea surfaces cause perturbations in the acquired seismic data. In addition to this, seismic streamer depths may also vary with time. However, static corrections applied to marine seismic data during processing are often inadequate and mainly consist of simple time shifting. This is because existing data processing algorithms assume that sea surface variations do not exist and that the data acquisition surface (streamers) is smoothly shaped and essentially horizontal. Such assumptions are mainly due to lack of precise information about the sea surface elevation and streamer depth variation.

In Figure 7, the dotted lines depict the ray path (green dotted lines), the sea surface (sky blue dotted line) and reference/datum streamer shape (yellow dotted line) usually assumed in processing marine seismic data. The continuous lines illustrate the true ray path (green line), the true sea surface (sky blue line) and the true streamer shape. All other ray paths have been ignored in Figure 7 for clarity. The shortened ray path travelled by the assumed wavefield (dotted green line) in reflecting from the flat sea surface coupled with the extra ray path it travelled to the reference streamer might cause miss-interpretations and miss-location of events, especially in case of time-lapse seismic. If true sea surface information and streamer depths are available (could be obtained by imaging the sea surface), these errors could be minimized.

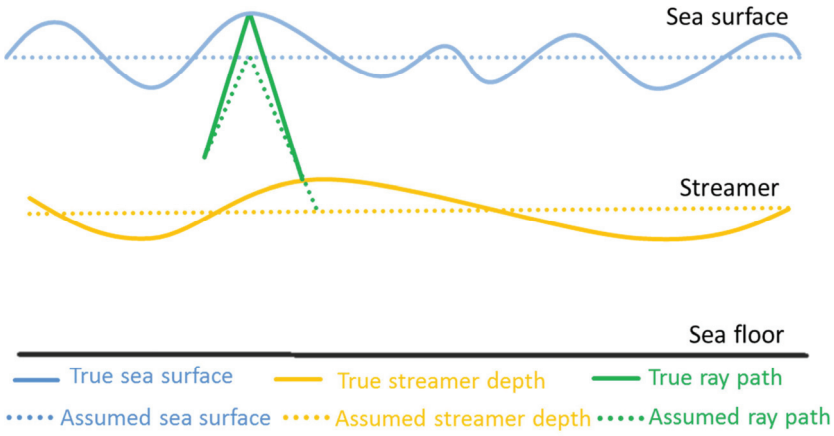

Figure 7: *A sketch depicting the ray path (dotted green line), flat sea surface (dotted sky blue line) and reference streamer depth assumed during data processing. The continuous lines show the true ray path (green line), the true sea surface (sky blue) and the true streamer depth.*

1.7 Time-lapse seismic

Employing an ensemble of streamers as in a 3D seismic data acquisition, has resulted in a better coverage of the subsurface, reduced the cost of acquiring data and lead to improved reservoir management (when repeated over time at the same location, 4D or time-lapse seismic data). In time-lapse seismic, successive images of a producing field aid geophysicists in identifying by-passed oil, however, the time-varying effects of the sea surfaces prove to be a bottleneck when these successive images are matched. This is because the sea surface condition changes with acquisition time. Figure 8 demonstrates how dramatic this can be for hydrophone-only-streamers. An initial shot gather of a seismic line was acquired under a flat sea surface condition (base survey) and then repeated under a rough sea condition (monitor survey). In Figure 8a (left part), the difference between the base and the monitor survey for a hydrophone-only-streamer is shown while Figure 8b (left part) shows the same for a collocated dual-sensor

streamer. Observe the large amplitude residue basically reflecting the sea surface fluctuations in Figure 8a (left part). Nevertheless, sea surface errors (caused by the source side ghost) are still present in Figure 8b (left part) and Figure 8a (left part). These errors are present because existing seismic processing and imaging methods assume flat and stationary sea surface conditions.

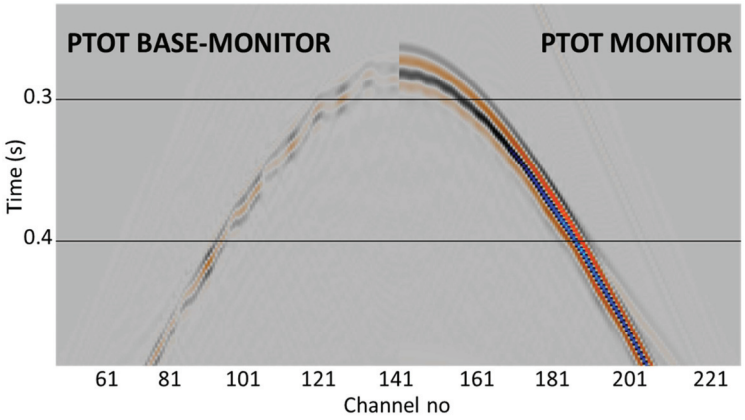

Figure 8a: *A shot gather showing total pressure wavefield for monitor survey (right) and the difference between base and monitor survey (left) for a time-lapse seismic survey carried out with a single source and a hydrophone-only-streamer. The residue seen on the left part of the plot is an error caused by both source and receiver sides' ghosts.*

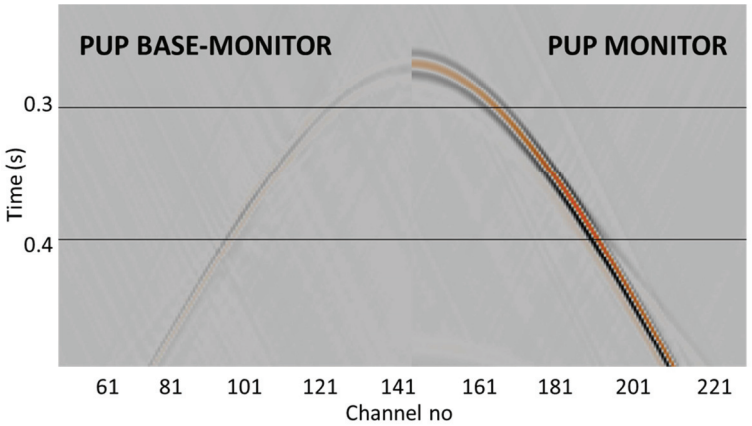

Figure 8b: *A shot gather showing total pressure wavefield for receiver side deghosted monitor survey (right) and the difference between base and receiver side deghosted monitor survey (left) for a time-lapse seismic survey carried out with a single source and a collocated dual-sensor streamer. The residue seen on the left part of the plot is an error caused by source side ghost.*

1.8 Objective of study and motivation

The objective of this study is to recover (image) realistic sea surface variations from acquired seismic data. Such information can be used in the future to improve the shortcomings in seismic processing already discussed (e.g., source ghost, surface related multiples, low-frequency compensation, streamer depth bias (varying streamer depth) and time-lapse seismic).

Presently, no robust and reliable method exists to obtain sea surface information from the acquired seismic wavefield. Thus the sea surface is normally assumed flat and stationary during seismic data processing. In recent times, attempts have been made to introduce deghosting techniques based on recorded sea-surface information. Laws and Kragh (2006) extracted sea surface elevation information from time varying pressure measurements using a specialized hydrophone set-up. However, this method is dependent on the precision of the pressure sensors

at very low frequencies (between 0.05-0.3 Hz) which is very well below normal seismic bandwidth. Alternatively, one may consider obtaining sea surface information from other remote sensing techniques like satellites. However, continuous sea surface information is not available using this technology. The main motivation of this thesis has therefore been to develop a reliable technique to recover continuous sea surface information from marine seismic data. This information will help mitigate the effects of marine seismic ghosts, surface related multiples, source and receiver depth fluctuation and rough sea errors on time-lapse seismic data.

The thesis work is divided into two main areas. Firstly, modeling techniques were developed to compute scattered seismic data from realistic time-varying sea surfaces. Such controlled data are vital when testing the proposed sea surface imaging technique. To represent realistic sea conditions, Pierson-Moskowitz type of spectra was employed (cf. Chapter 2). Secondly, a reliable technique for imaging or recovering a time-varying sea surface has been proposed and implemented (cf. Chapter 3). It is based on the concepts of wave decomposition, wave extrapolation and imaging. The feasibility of this method has been tested using controlled data. In addition, the imaging technique has been applied to several field data (both 2D and 3D) with good success.

Chapter 2

Realistic sea surface modeling and computation of scattered data

This chapter will briefly discuss: (i) how to model a realistic time-varying sea surface and (ii) how scattered data from such a time-varying surface can be computed.

2.1 Pierson-Moskowitz sea surface

In the absence of any artificial (e.g., ships) or natural sources (e.g., earthquakes), realistic sea surface waves (i.e., sea surface shape) are related to the prevailing wind. Wind-generated waves are surface waves that occur on the free surface. They are formed by the oscillation of water particles due to the frictional drag of wind over the water surface. These waves exhibit the typical characteristic of families of sinusoids with crests and troughs and covering a range of wavelengths and wave heights. Sea surface waves travel in groups called wave trains whose sizes depend on the wind velocity, fetch (area of the sea surface covered by the wind), the duration of the wind, friction on the water surface and the water depth. A low-velocity wind blowing over a large fetch first causes smaller waves called capillary waves or ripples to be formed. A sustained action of the wind with increasing intensity eventually generates larger sea

surface waves. These larger waves stabilize to form regular patterns of smooth, rounded waves called swells after the wind has slowed down or totally subsided. Wind-generated waves have certain amount of randomness (possessing waves with different heights, shapes and a limited predictability) and can be described as a stochastic process. The key statistical parameters characterizing the waves are the wave heights, wave periods (spatial wavenumbers) and the power spectra.

Wind wave models based on the spectra of the sea waves are used to predict the sea state. Perhaps the most popular wind wave model is the one described by Pierson and Moskowitz (Pierson and Moskowitz (1964)). They developed an empirical model that predicts the spatial spectrum from the prevailing wind speed and the spatial wavenumbers. Pierson and Moskowitz conceptualized a fully developed sea state as follows. Imagine a mirror-like smooth sea surface which is suddenly acted upon by a wind of a given speed. The turbulence in this wind produces random pressure fluctuations at the sea surface. This in turn produces small waves with wavelengths of a few centimeters (Phillips, 1957). As the wind continues blowing, bigger waves are formed. A sustained interaction of the wind and the waves produce pressure differences that cause some of the waves to continue growing. This process is unstable because, as these waves get bigger, the pressure differences also increases and the waves grow faster. This instability in the growth of the waves causes the waves to grow exponentially (Miles, 1957). Constructive and destructive interference among the waves produce longer waves (Hasselmann et al., 1973). This interaction transfers wave energy from short waves to waves with spatial frequencies slightly lower than the spatial frequency of waves at the peak of the spectrum. Eventually, this leads to waves (at the dominating wavelengths) travelling faster than the wind (Stewart, 2005).

Pierson and Moskowitz (1964) described this process by introducing the following power spectrum of the sea waves:

$$W(K_j, K_l) = \left[\alpha / (2 \mid K_{jl} \mid^3)\right] e^{-(\beta g^2)/(K_{jl}^2 U_w^4)}, \tag{2.1}$$

where K_j and K_l are respectively the x- and y- components of the absolute wavenumber $K_{jl} = \sqrt{K_j^2 + K_l^2}$, U_w is the wind speed (measured at a height of 19.5 m), α and β are constants of respectively 8.10×10^{-3} and 0.74 while g is the acceleration due to gravity. By assuming random relative phase shifts between each wavenumber component, the sea surface wave heights are obtained (see Thorsos, 1988; Orji et al., 2012). The upper panels of Figure 9 show a Pierson-Moskowitz sea surface (top left) for an isotropic wind blowing with a speed of 17 m/s together with the associated isotropic spectrum (top right). In order to correctly model the energy balance of the sea surface, an assumption about the angular distribution of the wave spectrum should be made. The simplest angular weight factor is $\cos^2(\theta)$, where θ represents the angular difference between the direction of a given wavenumber component and the prevailing wind direction. However, experimental studies indicate that the angular distribution is not only wavenumber dependent but also narrower near the peak wavenumber (Komen, Hasselmann and Hasselmann, 1984). Based on the evidence from their experiment, Hasselman et al., (1980) developed a directivity correction for an isotropic sea surface spectrum. The directivity correction is introduced as a multiplication between the sea surface spectrum in equation (2.1) and a directional term (see paper III; Hasselmann et al., 1980; Komen, Hasselmann and Hasselmann, 1984; Laws and Kragh, 2002). The lower panels in Figure 9 show the sea surface after directivity correction (bottom left) and the associated directional wavenumber spectrum (bottom right). Observe that the main wind driven events are now aligned in the specified direction of 90° as expected.

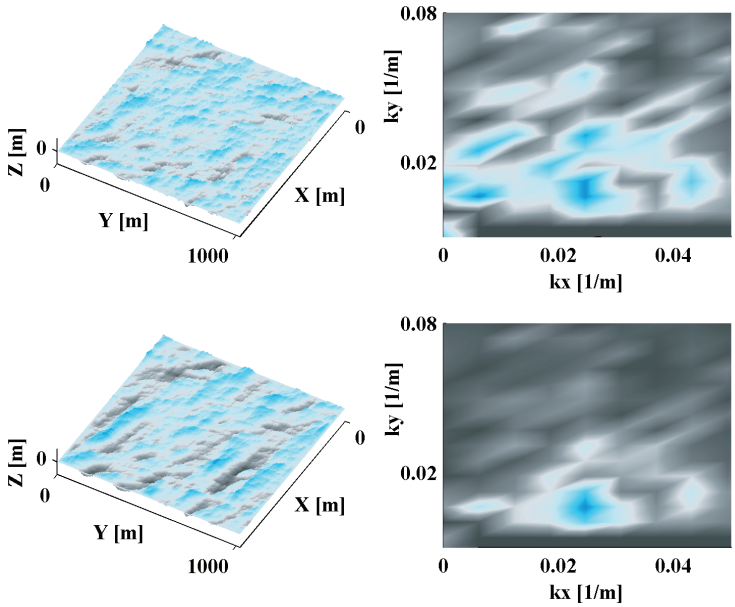

Figure 9: *Surface plots showing isotropic Pierson-Moskowitz sea surface for a wind blowing with a speed of 17 m/s with no specified direction (upper left) and the corresponding wavenumber spectrum (upper right). Directional Pierson-Moskowitz sea surface for a wind blowing with a speed of 17 m/s in the positive x-direction (lower left) and the associated spectrum (lower right). The wavenumber spectral plots have been zoomed to emphasize the wavenumber values.*

The procedure as illustrated in Figure 9 still describes a frozen rough sea surface. In order to make the sea surface propagate in the specified direction in a realistic manner, the deep water dispersion relation should be applied. This is because as sea surface waves propagate, they naturally separate according to their directions and wavelengths. The deep water dispersion relation reads:

$$\Omega_{jl} = \sqrt{gK_{jl}}, \tag{2.2}$$

where Ω_{jl} is the spatial angular frequency. Thus, by combining the directional Pierson-Moskowitz spectrum and the dispersion relation, time-varying realistic sea surfaces are simulated. This type of sea surfaces are employed in computing controlled data used in validating the sea surface imaging technology.

2.2 Scattering from a time-varying sea surface

Sea surface (rough surface) interaction with an incident acoustic wavefield has been described by many theories. Probably the first reported work is that of Rayleigh theory (Rayleigh, 1878). More recently, Kirchhoff (Eckart, 1953) and perturbation (Gilbert and Knopoff, 1960) theories have been introduced. Common among these theories is that they are calibrated based on the surface roughness (i.e., the resolvable sea surface wavelengths). For example, the perturbation method applies to relatively smooth surfaces whereas the Kirchhoff method and its extensions apply to rougher surfaces (Thorsos, 1990). In marine seismic data acquisition, a typical seismic bandwidth is about 5-125 Hz. This has a direct implication in terms of the resolvable sea surface spatial wavelengths. An acoustic wave with frequency f propagating through a medium (e.g., water in this case) with a propagation speed c has a wavelength given by $\lambda = \frac{c}{f}$. Thus, the obtainable sea surface spatial resolution is proportional to λ. To compute realistic scattered data from a rough sea surface, only surface roughness that lie within the seismic bandwidth must be properly accounted for.

Examples of possible candidates of modeling methods are: ray tracing method, the finite-difference method and the Helmholtz-Kirchhoff integral method. All these methods come with limitations because of their respective inherent assumptions. Ray tracing is suitable for smooth or flat sea surfaces because of its high frequency assumption. On the other hand, the finite difference method works for comparatively rougher interfaces. However the computational cost for more realistic rough sea surfaces and the difficulty in implementing time varying boundaries makes the finite difference technique less attractive. Perhaps the most robust and

computationally efficient method is the Helmholtz-Kirchhoff integral technique. It has been demonstrated to work for typical rough sea surfaces usually encountered in marine seismic data acquisition. Most importantly, it can be used to compute data in the case of time varying sea surfaces. This method was combined with Pierson-Moskowitz sea surfaces to efficiently model seismic experiments in this thesis work.

2.2.1 Helmholtz-Kirchhoff integral

Acoustic waves incident on a sea surface generate scattered wavefields. The scattered wavefields comprise of coherent (specular reflection) and incoherent (non-specular reflection) components. The type of scattering that dominates depends on the roughness of the sea surface. For a smooth sea surface, specular reflection dominates and vice versa. Scattered waves can be efficiently computed based on the Helmholtz-Kirchhoff integral (e.g. Holford 1981; Thorsos, 1988; Amundsen, 1994; Siderius and Porter, 2008; Orji et al., 2012) (2D case shown here):

$$P(\vec{r},\omega) = \frac{1}{4i} H_0^{(1)}(k\,|\,\vec{r}_d\,|)S(\omega) - \frac{1}{4i}\int_{\partial L}\left[H_0^{(1)}(k\,|\,\vec{r}\,' - \vec{r}\,|)\right]\frac{\partial P(\vec{r}\,',\omega)}{\partial n'}\,dl', \tag{2.3}$$

where $H_0^{(1)}$ is the zeroth-order Hankel function of the first kind, $S(\omega)$ is the source spectrum, k is the temporal wavenumber of the propagating wavefield, dl' is the length parameter along the rough surface, $|\vec{r}\,' - \vec{r}|$ defines the distance from the receiver location $\vec{r}$ to a scattering point $\vec{r}\,'$ on the sea surface and $|\vec{r}_d|$ is the distance from the "secondary" source to the receiver. Equation (2.3) represents the pressure wavefield recorded by a receiver located at (x_R, z_R) due to a wavefield emitted by a source located at (x_S, z_S) (see Figure 10). The total wavefield comprises of the incident pressure field (first term on the right hand side of equation (2.3)) and scattered pressure field (second term on the right hand side of equation (2.3)).

Kirchhoff approximation

In order to ensure an efficient computation of the scattered field (the integral on the RHS of equation (2.3)), the Kirchhoff approximation was employed here. Benchmarking using an exact method shows that the Kirchhoff approximation works well for the typical sea surface conditions and seismic bandwidths. The main idea behind this approximation is that the sea surface locally can be replaced by its tangent plane at the point of incidence and the planewave reflection coefficient can be used (Thorsos, 1988; Schleicher et al., 2007). As a consequence, the pressure gradient $\frac{\partial P(\vec{r},\omega)}{\partial n}$ in equation (2.3) can be replaced as follows: is obtained by assuming pressure release surface at the sea surface and employing numerical invasion. However, this process could be computationally expensive and also limits the solution to frozen sea surfaces only.

$$\frac{\partial P(\vec{r},\omega)}{\partial n} \cong \frac{2\partial P_{inc}(\vec{r},\omega)}{\partial n} \tag{2.4}$$

$P_{inc}(\vec{r},\omega)$ is the incident field at a scattering point on the sea surface. Thus, the scattered field can now be calculated with relatively less effort. In order to be able to handle a time-varying sea surface, the scattering problem is rather solved directly in the time-domain introducing time-delays honoring causality. Figure 10 shows a 2D Pierson-Moskowitz sea surface for a wind speed of 17 m/s (top panel) and the corresponding total pressure wavefield calculated along a line of 128 receivers located at a depth of 15 m below the sea surface. Observe that the direct or upgoing wavefield (the first event in the lower panel) is 180° out of phase with the scattered wavefield or downgoing wavefield (second event in the lower panel) as expected. We can also easily see the effect of the rough sea surface on the scattered waves.

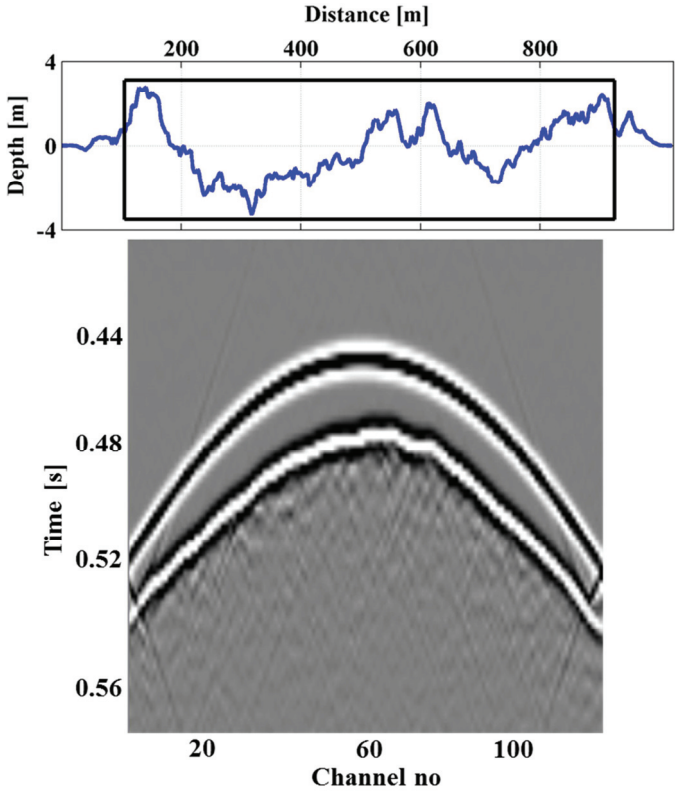

Figure 10: *Plot showing 2D Pierson-Moskowitz sea surface for a wind blowing with a speed of 17 m/s (top panel) and the corresponding total pressure field computed based on the Kirchhoff approximation for 128 receivers (bottom panel). The inset box shows that part of the sea surface covered by the streamer.*

Chapter 3

Sea surface imaging technology

To recover sea surfaces from synthetic or field data involves firstly a decomposition of the recorded data into its upgoing and downgoing components in a process termed "*wavefield separation*". Secondly, the decomposed wavefields are *extrapolated* upwards in small discrete steps until they coincide in time and space. Finally, an adequate *imaging condition* is applied to recover these positions of coincidence which essentially define the sea surface variations.

3.1 Wavefield separation

Collocated dual-sensors towed in an isotropic acoustic medium such as water, measure propagating pressure differences and particle velocities of the medium. These wavefields comprise of a series of compression and rarefactions with the direction of motion being parallel to the direction of propagation of the pressure wavefields. 2D planewave representation of the total pressure wavefield measurements of a sensor placed at a depth z_R can be written as:

$$P = U + D, \tag{3.1}$$

Making use of the relationship between the vertical particle velocity field and the pressure field (equation (1.5)), the velocity sensor will correspondingly record:

$$V_z = \frac{-dP}{i\rho\omega dz} = \frac{k_z(D-U)}{\omega\rho} = \frac{\cos\theta(D-U)}{\rho c}, \quad \Rightarrow D-U = \frac{\rho c V_z}{\cos\theta} \tag{3.2}$$

with θ being the angle of incidence. The vertical wavenumber k_z fulfills the following dispersion relation:

$$\frac{\omega^2}{c^2} = k_z^2 + k_x^2,$$

where k_x is the horizontal wavenumber associated with the inline or x-direction. This 2D formulation can easily be extended to 3D by including the cross-line or y-direction. The receiver side deghosted pressure field or upgoing wavefield is obtained by subtracting equation (3.2) from equation (3.1) and scaling with a factor of 0.5:

$$U = \frac{1}{2}(P - \frac{\rho c}{\cos\theta} V_z), \tag{3.3}$$

whereas the downgoing pressure wavefield is obtained from a simple addition of the collocated wavefield measurement (i.e., adding equations (3.2) and (3.1)) and scaling with 0.5:

$$D = \frac{1}{2}(P + \frac{\rho c}{\cos\theta} V_z), \tag{3. 4}$$

If we now consider the special case of vertical incidence ($\theta = 0$), the measurements from the two sensors will then be in phase in the direction of the propagation and the constant of proportionality relating the two measurements is now only the acoustic impedance factor ρc. Since the positive $z-$axis is downwards, the signals of energy propagating in the downward

direction are in phase for the two sensors, while the signals of energy propagating in the upward direction (i.e., negative $z-$axis) are 180° out of phase. Figure 11 depicts wavefield separation for a source deghosted wavefield arriving vertically at the collocated dual-sensors. In Figure 11, the ghost recorded by the pressure sensor (and particle velocity sensor) is portrayed as having equal magnitude as the upgoing event. This is because the sea surface has been assumed to be flat for simplicity of the illustration. Nevertheless, the nature of the sea surface does not in principle affect wavefield separation (e.g., Fokkema and van den Berg, 1993; Scholmeesters, 2001).

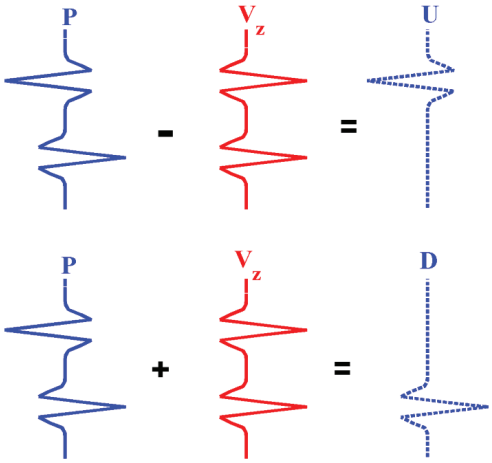

Figure 11: *Plots illustrating wavefield separation as a simple dual sensor subtraction with proper scaling to obtain the upgoing pressure wavefield U (upper panel) and a dual sensor summation with proper scaling to obtain the downgoing pressure wavefield D (lower panel)*

3.2 Wavefield extrapolation

The main purpose of wave field separation is to be able to extrapolate (move) the decomposed wavefields to any chosen depth. In order to image the sea surface, the separated upgoing and downgoing wavefields are moved upwards from the sensors' depth levels towards the sea surface

in small discrete steps. The principle of the extrapolation can be explained starting from the general solution of the Helmholtz equation (equation (1.5)):

$$P = U + D = Ae^{i(k_z z)} + Be^{i(-k_z z)} \tag{3.5}$$

Considering now only upward propagating waves in equation (3.5) (i.e., $B = 0$), the pressure wavefield at receiver depth $z = 0$ may be used to find the constant A:

$$U(k_z, z = 0, \omega) = A \tag{3.6}$$

Similarly, for the upwards propagating wavefield at an arbitrary observation depth $z = z_1$, one obtains from equation (3.5):

$$U(k_z, z_1, \omega) = U(k_z, z = 0, \omega)e^{i(k_z z_1)} \tag{3.7}$$

The upgoing pressure wavefield at the receiver depth $z = z_R$ is then:

$$U(k_z, z_R, \omega) = U(k_z, z = 0, \omega)e^{i(k_z z_R)} \tag{3.8}$$

Therefore, the extrapolation of the upgoing wavefield upwards from depth z_R to depth z_1 is achieved by combining equations (3.7) and (3.8):

$$U(k_z, z_1, \omega) = U(k_z, z_R, \omega)e^{-ik_z(z_R - z_1)} \tag{3.9}$$

The upward (towards the sea surface) extrapolation of the downgoing wavefield is obtained by setting $A = 0$ in equation (3.5). If we denote now the measured upgoing and downgoing pressure fields at the receiver level by U_R and D_R respectively, the upgoing wavefield is extrapolated from the sensor depth level z_R to another depth z_1 by applying the following equation:

$$U_1 = U_R e^{ik_z(z_1 - z_R)}, \tag{3.10}$$

whereas the downgoing wavefield is taken to the same depth by the operation:

$$D_1 = D_R e^{ik_z(z_R - z_1)}, \tag{3.11}$$

where U_1 and D_1 respectively denote the upgoing and downgoing wavefields vertically extrapolated to the depth z_1. Similar expressions can be written for the vertical particle velocity wavefields.

Initially, the time difference between upgoing and downgoing wavefields is given by the ghost period (time taken for the wavefield to reach the sea surface and propagate back again to the sensor), as the extrapolation continues, this ghost period reduces with each extrapolation step until it is zero at the sea surface where the upgoing going and downgoing wavefields coincide in time. A summation of the amplitudes of the two wavefields at this point of coincidence gives zero in the case of a flat sea surface. This is because at the flat sea surface, the two wavefields have the same magnitude and are 180° out of phase because of the reflection coefficient of -1 at the sea surface. Figure 12 illustrates vertical extrapolation of the separated upgoing and downgoing wavefields from the original receiver depth to an assumed flat sea surface (at 0 m). In reality, a line(s) of sensors (streamer) is usually considered. Streamers are usually not flat during data acquisition because of its weight. Therefore, the depth variations of the sensors must be taken into account (see Fokkema and van den Berg, 1993; Söllner et al., 2008; Orji, 2009). The extrapolation step-size (in depth) must be chosen such that the smallest sea surface wave height variations that can be resolved by the seismic wavefield are captured. Tests using different extrapolation step-sizes show that step-size of 0.1 m is sufficient for marine seismic case (very short sea surface wavelengths are usually filtered by the seismic wavefield). Upward extrapolation of the upgoing and downgoing wavefields is continued until these two wavefields coincide in time and space. The position (coordinate) of the coincidence defines the sea surface position.

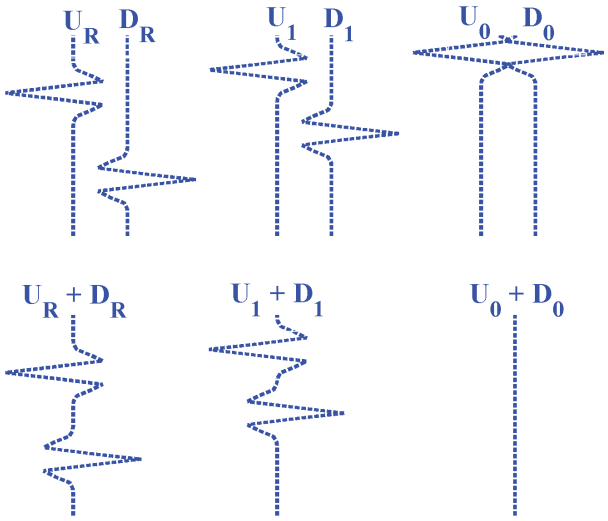

Figure 12: *Plots illustrating extrapolation of the upgoing U_R and the downgoing D_R pressure wavefields: from sensor depth (upper panel left) to an arbitrary depth (upper panel middle) and then to the sea surface depth (upper panel right.) Lower panels: summation of the extrapolated wavefields at each depth. The sum of the amplitudes of the extrapolated wavefields at the sea surface is zero.*

3.3 Imaging condition

In order to extract the positions of coincidence an imaging condition must be employed. Conventional seismic imaging is based on the assumption that wavefields originating from a seismic source propagate to and interact with a discontinuity as an incident wavefield before returning to a receiver(s) as a reflected seismic wavefield (Berkhout, 1982; Claerbout, 1985; Sava and Vlad, 2011). Thus, the two wavefields (i.e., incident and reflected wavefields) kinematically coincide at the discontinuity (in our case a sea surface point). Therefore, the key elements in imaging the sea surface point are the incident (upgoing wavefields) and reflected wavefields (downgoing wavefields). These wavefields are first propagated upwards to the point

(space) and time where they interacted with the sea surface point by employing wavefield extrapolation. This procedure can be carried out in the space-time domain, the wavenumber-frequency domain or the space-frequency domain. Then an adequate imaging condition is applied to extract the point of coincidence (sea surface) and the amplitude value at the image point can be further analyzed for the possibility of extracting sea surface reflectivity information.

A conventional cross-correlation imaging condition is formulated as the zero-lag of the cross-correlation between the upgoing and downgoing wavefields (Claerbout, 1985). Classical imaging condition employs a division of the reflected wavefield by the source wavefield (Claerbout, 1971). A comparison of different types of imaging conditions has been carried out by Schleicher et al., (2008) and Vivas et al., (2009). From these reviews least-squares type of imaging conditions have been shown to be most robust. Such a condition involves a division of the cross-correlation of the upgoing and dowgoing wavefields by the autocorrelation of the upgoing wavefields at each extrapolation depth:

$$I(x_1, z_1) = \frac{\sum_{\omega} U_1(x_1, z_1, \omega)\overline{D_1(x_1, z_1, \omega)}}{\sum_{\omega} U_1(x_1, z_1, \omega)\overline{U_1(x_1, z_1, \omega)}} \tag{3.12}$$

I indicates the image point amplitude and its coordinate (x_1, z_1) defines the current receiver position (x_1) and the extrapolation depth (z_1). The calculation is performed within a selected window of traces (selected line of receivers).

Figure 13 shows plots of the numerator of equation (3.12) for different extrapolation depths (from 3 m with step-size 0.1 m to -3 m with 0 m representing the datum) for four selected receivers (number 16, 32, 64 and 96) from a streamer containing 128 receivers. The seismic cable was placed at a depth of 15 m and the same Pierson-Moskowitz sea surface as shown in Figure 10 was employed. The peak of each plot indicates the sea surface depth position for the given receiver. Figure 14 shows plots of the corresponding denominator of equation (3.12). The zero-lag amplitude values of the autocorrelations show only marginal changes with extrapolation

depths as expected. The minor linear trend seen in Figure 14 is because of the difference in the geometrical spreading for different depths (i.e., amplitude decreases with increasing upward extrapolation of the upgoing wavefield). In Figures 13 and 14, the computed correlations for a given depth (i.e., for a given receiver) were not normalized. The normalization (done only for visualization purpose here) in the plots were computed using the peak amplitudes for all the depths considered for a given receiver.

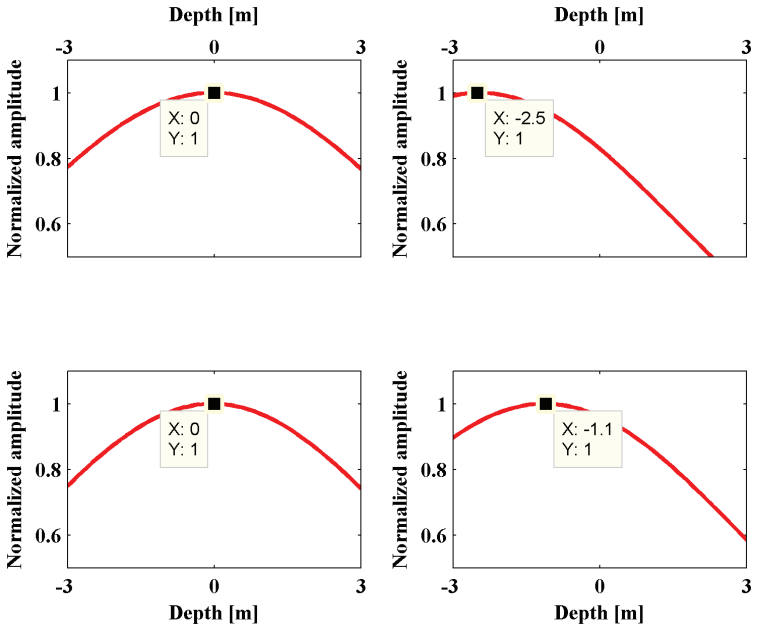

Figure 13: *Plots showing cross-correlation of upgoing and downgoing wavefields at different extrapolations depths for receiver: 16 (upper left), 32 (upper right), 64 (lower left) and 96 (bottom right) from a streamer containing 128 receivers. In the calculations, a 2D Pierson-Moskowitz sea surface with wind blowing at a speed of 17 m/s is assumed (see also Figure 10). Extrapolation depths corresponding to peak values are indicated for each receiver.*

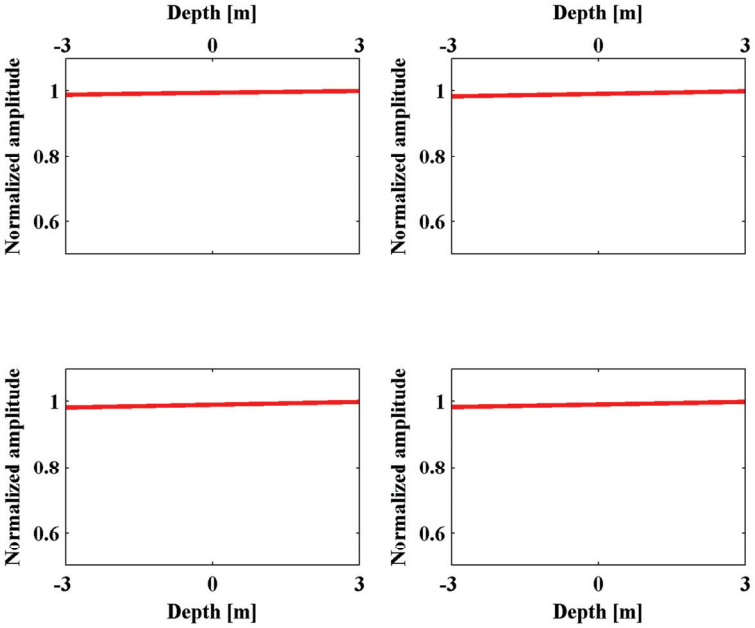

Figure 14: *Plots showing auto-correlation of upgoing wavefields at different extrapolations depths for receiver: 16 (upper left), 32 (upper right), 64 (lower left) and 96 (lower right) from a streamer containing 128 receivers. In the calculations, a 2D Pierson-Moskowitz sea surface with wind blowing at a speed of 17 m/s is assumed (see also Figure 10).*

Figure 15 shows the extracted extrapolation depths corresponding to peak values for each receiver position. These points give a reconstruction of the modeled Pierson-Moskowitz sea surface shown earlier in Figure 10. Note the good match between the modeled sea surface (blue) and the imaged sea surface (red). However, because of the band limited source pulse used in computing the data, the imaged sea surface is a filtered version of the modeled sea surface. A repetition of this process in a sliding window through the data gives different sea surface profiles corresponding to different times and the time variable characteristics of the sea surface is then extracted.

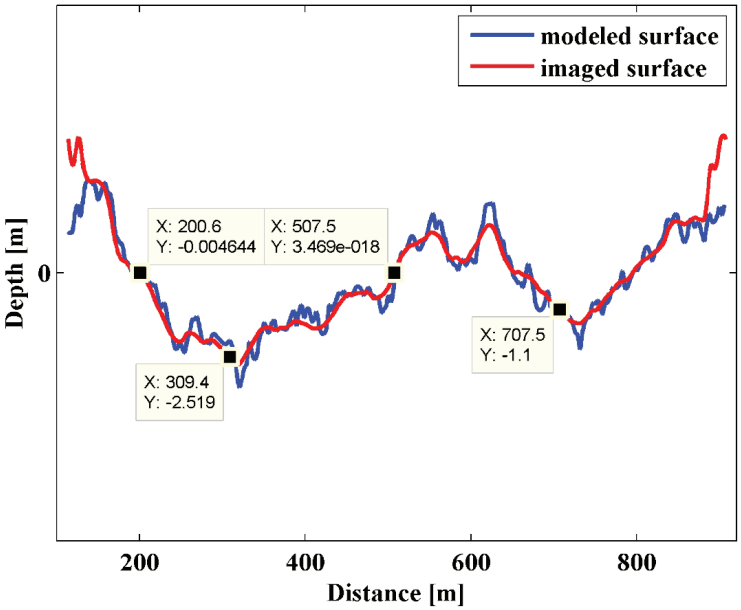

Figure 15: *Plot showing modeled (blue) and imaged Pierson-Moskowitz sea surface (confirm from the black inset box in Figure 10). The corresponding receivers' positions* (x) *(starting from receiver16 and ending in receiver 96) and the corresponding extrapolation depths* (z) *with peak amplitude values of the cross-correlations for these receivers are also shown (cf. Figure 13).*

Chapter 4

Main scientific contribution

Sequel to the sea surface imaging patent (PGS-08-04US) the overall goal of this PhD work has been to investigate the feasibility of obtaining the time-variant sea surface shape and the associated reflection coefficient estimates from decomposed dual-sensor streamer data. Encouraged by the results obtained from the early feasibility studies a series of improvements were proposed and implemented to demonstrate the ability of the technique to reconstruct realistic time-variant sea surfaces from 2D and 3D dual sensor seismic data. Due to limited time, recovering of actual reflectivity information was only partly investigated. Since this PhD work has been funded through an industrial type of PhD grant, we have also included a summary of two patents developed through the project. However, the academic part of this work consists of three journal papers of which two have already been published in Geophysics. The third paper is currently being reviewed by the same journal.

4.1 Summary of publications

4.1.1 Paper I

Orji O. C., W. Söllner and L-J. Gelius, 2010, Imaging the sea surface using dual-sensor towed streamer: Geophysics **75**, P. V111 – V1118.

Paper I reports a feasibility study of sea surface imaging using dual-sensor towed streamer. In the first part of the study, controlled data were computed based on ray tracing assuming a flat and stationary sea surface. The imaging technology was then calibrated with respect to noise, extrapolation step-size and imaging window size. The possibility of extracting reliable sea surface reflection coefficient estimates was also demonstrated in the case of this flat sea surface. In the second part of the study, time-domain finite-difference modeling was employed to compute scattered data from a comparatively rougher "frozen" sea surface comprising of a composite of sinusoids. Encouraged by the good result obtained for the rough sea surface situation, the technique was then employed in a sliding window mode to obtain time-varying sea surfaces from a shot gather taken from field data acquired under marginal weather condition offshore North Sea. The feasibility study was carried out employing synthetic data associated with simple 1D sea surfaces and also many effects encountered in marine seismic acquisition (e.g., moving receivers, time-variant sea surfaces etc.,) were not included in the study because of lack of proper modeling tools at that time.

4.1.2 Paper II

Orji O. C., W. Söllner and L-J. Gelius, 2012, Effects of time-varying sea surface in marine seismic data: Geophysics **77**, P33-P43.

In paper II the main focus was on developing a forward modeling tool that computes scattered data from realistic sea surfaces. A 1D time-varying Pierson-Moskowitz sea surface formulation was developed and forward modeling based on the 2D Helmholtz-Kirchhoff integral (with and without Kirchhoff approximation) able to compute scattered data from the time-varying sea surfaces was developed. The forward modeling tool included possible effects caused by moving streamers and streamers with variable shape. Effect of moving receivers was shown to be a lateral translation of the imaged sea surface whereas variable streamer depth caused a vertical displacement of the imaged sea surface. Spectral analyses of the sea surfaces were also carried out and the speeds of the main-wind-driven events of the sea surfaces were shown to be related to the spectral peaks. Four consecutive shots from field data acquired under marginal weather condition from North Sea were imaged. The imaged time-varying sea surfaces show similar spectrum and thus, approximately the same speed as expected. However, the modeled sea surfaces employed in the validation tests of the imaging technique were still formulated in 1D.

4.1.3 Paper III

Orji O. C., W. Söllner and L-J. Gelius, 2012, 2D time-varying sea surface imaging using 3D towed dual-sensor streamers: Geophysics (Revised version submitted July 2012)

Encouraged by the results obtained in paper II, further validation tests were carried out to fully demonstrate the robustness of the imaging technique in paper III. The forward modeling tool was extended to 3D and the sea conditions considered were in the form of 2D time-varying Pierson-Moskowitz sea surfaces including Hasselmann's directivity correction. The possibility of using the imaging technique to obtain 2D sea surfaces from sparsely spaced dual sensor 3D data was demonstrated by applying the imaging technique to 3D controlled data. The imaging technology was first applied in 3D and then in 2D (i.e., streamer-wise). The robustness of the technique was demonstrated by showing that it can resolve the main features of a given sea surface when applied in 2D for different sparse streamer spacing (e.g., 25 m, 50 m and 100 m). The speeds and directions obtained by carrying out spectral analysis of the imaged sea surfaces were used to further validate these results. First 2D time-varying sea surfaces were obtained from field data acquired from two different locations (offshore Brazil and North Sea) and under different weather situations (moderate and marginal weather conditions respectively). The recovered wave heights, speeds and directions from the field data were plausible.

4.2 Summary of current patent applications

4.2.1 Patent I

Methods and Systems for Correction of Streamer-Depth Bias in Marine Seismic Surveys

(PGS-11-44US)

The disclosure involves estimating and correcting for streamer-depth bias in marine seismic surveys. It can be viewed as a way of carrying out the needed marine static corrections. This is achieved by carrying out spectral analyses of imaged sea surfaces. Ideally, for sea surfaces covering sufficiently large areas, the speeds and directions of the main-wind-driven events are related to their spectral peak wavenumbers provided the sea surface profiles were obtained using their correct streamer depths. However, if the wrong streamer depths were used in imaging the sea surfaces, strong artifacts close to zero wavenumbers will be present in the respective spectra. The correct streamers depths are obtained by finding streamer depths that minimizes/removes the artifacts in the spectra.

4.2.2 Patent II

Methods and Systems for Reconstruction of Low Frequency Particle Velocity Wavefield and Deghosting of Seismic Streamer Data

(PGS-11-51US)

This disclosure includes compensating for the frequencies lost because the velocity sensor measurement is swamped by noise at low frequencies. These low frequencies are reconstructed by first computing free surface wavefield reflectivity (Green's function) at every receiver position based on Helmholtz-Kirchhoff integral employing the previously imaged sea surface (free surface). The free surface on the source side is obtained by backward propagating the imaged sea surface in order to obtain the sea surface at the time the source was fired. This is

achieved by exploiting deep water dispersion relation. Pressure wavefields are obtained from the field measurements. Armed with these parameters, Fredholm integral equation of the first kind is solved to obtain the pressure gradient. Finally, the vertical particle velocity wavefields are then reconstructed for those "missing" frequencies based on the relationship between velocity wavefield and pressure gradient. This is for the case where the source is towed at a depth above the streamers. If the source is towed below the streamers, then the Fredholm integral is slightly modified (source side free surface and the reflectivity are not needed)

Chapter 5

Summary and future work

5.1 Summary

The studies presented here, is focused on recovering the time-variant sea surface shape from scattered dual sensor data. The work evolved gradually following a "work breakdown" structure. It started with 1D frozen flat sea surfaces where 2D ray tracing was used to compute controlled data. It then progressed to 1D frozen rough sea surfaces constructed from a composite of sinusoids where 2D time-domain finite-difference modeling was used to compute scattered data from the sea surface. Encouraged by the results obtained from both synthetic and field data, 1D time-varying realistic sea surfaces based on the Pierson-Moskowitz formulation were then investigated. More efficient forward modeling tools in the form of the 2D Helmholtz-Kirchhoff integral (with and without the Kirchhoff approximation) able to handle time-varying boundary conditions were also developed. Then effects of moving streamers and variable streamer depths were incorporated in the forward modeling and investigated through imaging. Subsequently, in order to model realistic marine seismic experiments as efficiently as possible, 2D time-varying directional Pierson-Moskowitz sea surfaces were investigated by employing the 3D Helmholtz-Kirchhoff integral to generate controlled data. Spectral analyses of the imaged sea surfaces were

carried out to determine the speeds and directions of the moving sea surfaces. Effects of sparse streamer spacing were then investigated. The robustness of the imaging technology was clearly demonstrated by presenting 2D time-varying sea surfaces obtained from two different field data.

5.2 Future work

Future work will be geared towards recovering robust estimates of the time-variant sea surface reflectivity. The feasibility of obtaining reliable sea surface reflection coefficient estimates for 1D frozen flat sea surfaces has already been demonstrated. Furthermore, sea surface reflectivity estimates recovered from a 1D sinusoidal surface is currently undergoing investigation. The reflectivity estimates obtained from this deterministic sea surface can easily be benchmarked since an analytical solution exists. Then statistical methods will be employed to investigate reflectivity estimates for realistic sea surfaces such as formulated by Pierson and Moskowitz. The imaging condition should also be reformulated in the planewave domain in order to be able to obtain and analyze the angle dependent sea surface reflectivity. If successful, such reflectivity information (in combination with the sea surface shape) can be useful for several applications as briefly discussed in section 5.2.1.

5.2.1 Possible future applications

Low frequency compensation (LFC)

In the low frequency compensation equation the sea surface reflectivity is needed. However, in current implementation the reflection coefficient is assumed to be -1 implying a flat and stationary sea surface. The general LFC equation (1.2) can directly be used (instead of the current version in equation (1.3)) if true sea surface reflectivity estimates were available.

Deghosting solutions

In an effort to remove sea surface ghosts, anti-ghost filters based on the assumption of a flat and stationary sea surface are employed. However, the actual sea surface profile and corresponding reflection coefficient estimates are important input parameters in case of a successful rough sea deghosting solution. A new generation of deghosting techniques can therefore be foreseen based on imaging technology presented in this work.

Surface related multiples elimination

Sea surface reflectivity estimates are also required in order to properly remove sea surface related multiples. This combined with proper source side deghosting and enhanced wavefield separation by employing a high-fidelity LFC might greatly improve time-lapse seismic imaging.

References

Amundsen L., 1993, Wave-number-based filtering of marine point source data: Geophysics, **58**, 1335-1348.

Amundsen, L., 1994, The propagator matrix related to the Kirchhoff-Helmholtz integral in inverse wavefield extrapolation: Geophysics, **59**, 1902–1910.

Amundsen L., B. G. Secrest, and B. Arntsen, 1995, Extraction of the normal component of the particle velocity from marine pressure data: Geophysics, **60**, 212-222.

Barr, F. J., and J. I. Sanders, 1989, Attenuation of water column reverberations using pressure and velocity detectors in a water-bottom cable: Expanded Abstracts of the 59th Annual SEG Meeting, Dallas, TX, 653-656.

Berkhout, A. J., 1982, Seismic migration: imaging of acoustic energy by wavefield extrapolation: Elsevier Science Publishers.

Claerbout, J. F., 1971, Fundamentals geophysical data processing: Blackwell Scientific Publications.

Claerbout, J. F., 1976, Fundamentals of geophysical data processing: McGraw-Hill.

Claerbout, J. F., 1985, Imaging the Earth's Interior: Blackwell Scientific Publications.

Eckart, C., 1953, The scattering of sound from the sea surface: J. Acoust. Soc. Am. **25**, 566-570.

Fokkema, J. T., and P. M. van den Berg, 1993, Seismic Applications of acoustic reciprocity: Elsevier Science Publ. Co.

Ghosh, S. K., 2000, Deconvolving the ghost effect of the water surface in marine seismics: Geophysics, **65**, issue 6.

Gilbert F and Knopoff L 1960 J. Geophys. Res., **65**, 3437-44.

Hasselmann K., T.P. Barnett, E. Bouws, H. Carlson, D.E. Cartwright, K. Enke, J.A. Ewing, H. Gienapp, D.E. Hasselmann, P. Kruseman, A. Meerburg, P. Mller, D.J. Olbers, K. Richter, W. Sell, and H. Walden, 1973, Measurements of wind-wave growth and swell decay during the Joint North Sea Wave Project (JONSWAP): Ergnzungsheft zur Deutschen Hydrographischen Zeitschrift Reihe, A(8) (Nr. 12), 95.

Hasselmann, D. E., M. Dunckel and J. A., Ewing, 1980, Directional wave spectra observed during JONSWAP 1973, J. Phy. Oc. **10,** 1264-1280.

Hegna, S., and P., Gregg, 2011, An acquisition system that extracts the earth response from seismic data: First break, **29**, 81-87.

Holford, R. L., 1981, Scattering of sound waves at a periodic, pressure-release surface: An exact solution, J. Acoust. Soc.Am. **70**, 1116–1128.

Komen, G.J., K. Hasselmann and S. Hasselmann, 1984, On the existence of a fully developed wind sea spectrum: J. Phys. Oceanogr. **14**, 1271-1285.

Laws, R., and E. Kragh, 2006, Sea surface shape derivation above seismic streamer: Section II Rhodes Worskshop 2004, Geophysical Prospecting, **54**, 817–828.

Miles J.W., 1957, On the generation of surface waves by shear flows: Journal of Fluid Mechanics: **3(2)** 185–204.

Orji, O., 2009, Imaging the sea surface from towed dual-sensor streamer data: Master thesis, UiO, DUO.

Orji, O., W. Söllner, and L. J. Gelius, 2012, Effects of time-varying sea surface in marine seismic data: Geophysics **77**, 33-43.

Parkes, G. and S. Hegna, 2011, Acquisition system that extracts the earth response from seismic data: First Break **29,** No 12.

Phillips, O.M., 1957, On the generation of waves by turbulent wind: Journal of Fluid Mechanics **2 (5)**, 417–445.

Pierson, W. J., and L. Moskowitz, 1964, A proposed spectral form for fully-developed wind seas based on the similarity theory of A. A. Kitaigorodskii, J. Geophys. Res., **69**, 5181-5190.

Posthumus, B. J., 1993, Deghosting using a twin streamer configuration: Geophysical prospecting **41**, 267-286

Rayleigh L., 1878, The theory of sound: **2,** London, Macmillan, 1st edn.

Sava, P., and I Vlad, 2011, Wide-azimuth angle gathers for wave equation migration: Geophysics, **76**, S131-S141.

Schleicher, J., M. Tygel and P. Hubral, 2007, Seismic true-amplitude imaging: Geophysical Developments, **12**.

Schleicher, J., J. Costa and A. Novais, 2008, A comparison of imaging conditions for wave-equation shot-profile migration: Geophysics, **73**, S219-S227.

Schneider, A. W., K. L. Larner, J. P. Burg, and M. M. Backus, 1964, A new data-processing technique for the elimination of ghost arrivals on reflection seismograms: Geophysics, **29**, 783–805.

Schoolmeesters, J. W., 2001, Three-dimensional processing of marine seismic data by spectral decomposition, ISBN 90-9014856-6, pg. 180.

Sheriff, R. E., 1991, Encyclopedic dictionary of exploration Geophysics, third edition: Soc. Expl. Geophys..

Siderius, M., and M. B. Porter, 2008, Modeling broadband ocean acoustic transmissions with time-varying sea surface, J. Acoust. Soc. Am. **143**, 137.

Stewart, H. R., 2005, Introduction to physical oceanography: Dept. of ocean. Texas, A and M Uni..

Söllner, W., A. Day and H. Tabti, 2008, Space-frequency domain processing of irregular dual-sensor streamer data: SEG Expanded Abstracts, **27**, 1078-1082.

Thorsos, E. I., 1988, The validity of the Kirchhoff approximation for rough surface scattering using a Gaussian roughness spectrum, J. Acoust. Soc. Am. **83**, 78–92.

Thorsos, E. I., 1990, Acoustic scattering from a "Pierson-Moskowitz" sea surface, J. Acoust. Soc.Am. **88**, 335–349.

Vivas, A. F., R. C. Pestana and B. Ursin, 2009, A new stabilized least-squares imaging condition: Journal of Geophysics and Engineering, **6**, 264-268.

Ziolkowski, A., 1971, Design of a marine seismic reflection profile system using airguns as a sound source: Geophys. J. Roy. Astr. Soc. **23**, 499-530.

Schoolmeesters, J. W., 2001, Three-dimensional processing of marine seismic data by spectral decomposition, ISBN 90-9014856-6, pg. 180.

Paper I

Imaging the sea surface using dual-sensor towed streamer

Orji O. C., W. Söllner and L-J. Gelius

Geophysics 75, P. V111 – V1118

GEOPHYSICS, VOL. 75, NO. 6 (NOVEMBER-DECEMBER 2010); P. V111–V118, 13 FIGS.
10.1190/1.3496439

Imaging the sea surface using a dual-sensor towed streamer

Okwudili Orji[1], Walter Söllner[2], and Leiv Jacob Gelius[3]

ABSTRACT

Sea-surface profile and reflection coefficient estimates are vital input parameters to various seismic data processing applications. The common assumption of a flat sea surface when processing seismic data can lead to misinterpretations and mislocations of events. A new method of imaging the sea surface from decomposed wavefields has been developed. Wavefield separation is applied to the data acquired by a towed dual-sensor streamer containing collocated pressure and vertical particle velocity sensors to obtain upgoing and downgoing wavefields of the related sensors. Time-gated upgoing and downgoing wavefields corresponding to a given sensor are then extrapolated to the sea surface where an imaging condition is applied so that the time-invariant shape of the sea surface can be recovered. By sliding the data time-window, the temporal changes of the sea surface can be correspondingly estimated. Ray tracing and finite-difference methods were used to generate different controlled data sets used in this feasibility study to demonstrate the imaging principle and to test the image accuracy. The method was also tested on a first field data example of a marginal weather line from the North Sea.

INTRODUCTION

A prerequisite for discovering any oil/gas reservoir is a well-resolved seismic image of the subsurface. In marine seismic data acquisition, streamers containing hydrophones (pressure sensors) are towed at a certain depth below the sea surface. The contact between water and air acts like a strong reflector generating the source and the receiver ghosts (Ghosh, 2000). The overlap of ghosts with subsurface reflections may interfere destructively and compromise the interpretability of the seismic events. In the frequency domain, the ghosts generate a pattern of undesired notches that affect the data resolution. The shape of the ghost pattern is influenced by the sea-surface topography and the sea-surface reflection coefficient. Until the present advancement in towed marine seismic surveying, the sea-surface topography has largely been assumed flat (with reflection coefficient -1) in data processing. Because the energy reflected from the sea surface is dependent on its condition, the effect of a rough sea on a seismic image can be quite dramatic compared with a calm sea. Laws and Kragh (2002) discuss the effects of rough seas on time-lapse seismics. Goto et al. (2008) describe the influence of the sea-surface shape as elevation statics on the source side and as a timing perturbation in the receiver ghost.

Traditional deghosting of seismic data is not a trivial procedure, even for a flat sea surface. This is because of the zeros in the spectrum of the ghost filter (Ghosh, 2000). Consequently, there is a limit in depth to which conventional streamers (i.e., with pressure sensors only) can be towed. If the streamer is towed at a shallow depth, low frequencies are attenuated, whereas a deep tow attenuates high frequencies. Improving the resolution of the acquired seismic data by flattening the spectral response and increasing the bandwidth at low and high frequencies require accurate deghosting schemes.

The statistical deconvolution approach as applied by Kragh and Laws (2001) is limited by the time-variant nature of the sea surface. In recent years, attempts have been made to introduce techniques for rough sea deghosting using sea-surface profile information. Kragh et al. (2002) demonstrated how the sea-surface profile can be derived using very-low-frequency (below 0.5 Hz) pressure fluctuations recorded by a special sensor setup of calibrated broad-band single-sensor hydrophones. Robertsson and Kragh (2002) utilized Lax-Wendroff correction to derive equations for vertical pressure gradient approximation along a streamer in the vicinity of a rough sea surface. The estimated pressure gradient and measured raw pressure data are used to deghost measured seismic data by applying the principle of wavefield separation. This method works best for low frequencies or shallow tow depth and is strictly limited to frequencies below the first ghost notch. An improved pressure gradient approximation is achieved by Amundsen et al. (2005) by applying a binomial series expansion on the exact relation between the vertical velocity field and pressure field (derived for a flat sea surface and reflection coefficient of -1). Both deghosting methods suffer from the fact that the

Manuscript received by the Editor 2 February 2010; published online 8 December 2010.
[1]University of Oslo, Department of Geosciences and Petroleum Geo-Services, Oslo, Norway. E-mail: okwudilo@student.geo.uio.no.
[2]Petroleum Geo-Services, Lysaker, Norway. E-mail: walter.sollner@pgs.com.
[3]University of Oslo, Department of Geosciences, Oslo, Norway. E-mail: l.j.gelius@geo.uio.no.

velocity field (one needed component of the dual wavefield) is approximated from the measured pressure field.

In contrast, the dual-sensor streamer comprising collocated hydrophones and particle velocity sensors measures the pressure and vertical particle velocity wavefields. A combination of these two wavefields can be used to perform wavefield separation (Tenghamn et al., 2007). The pressure field is decomposed into upgoing and downgoing pressure wavefields, whereas the vertical velocity field is decomposed into upgoing and downgoing vertical particle velocity wavefields. Both decompositions are performed independent of the sea-surface condition. Thus, in principle, the dual-sensor streamers can be towed at any depth compared with conventional streamers that are normally towed between 6- and 9-m depths. The upgoing wavefields of either of the sensors are equivalent to receiver deghosted data with flat spectra at any cable tow depth and are generally leading to an improved image resolution (Carlson et al., 2007). The scattered downgoing wavefields containing the sea-surface effects represent the receiver ghost. Removing all sea-surface effects is the goal of surface-related multiple elimination (SRME) (Verschuur, 1991, Berkhout and Verschuur, 1997) and related methods of surface-related multiple suppression (Carvalho et al., 1991; Fokkema and van den Berg, 1993; van Borselen et al., 1996; Amundsen, 2001, Ikelle et al., 2003). A common feature of these methods is the independency of parameters characterizing the subsurface model. However, sea-surface influence in shape and reflection coefficient is commonly ignored. To relax the sea-surface assumptions of SRME, Söllner et al., 2007 and Frijlink et al., 2009 use the downgoing velocity field in combination with the upgoing pressure field as a sea-surface multiple generator.

It turns out that the scattered downgoing wavefield containing the sea-surface reflectivity plays a fundamental role in the seismic inversion process (Berkhout et al., 2009). To our knowledge, no attempt has been reported so far to determine the sea-surface reflectivity operator from the seismic wavefield. Instead, a unity matrix, the flat stress free surface assumption, largely replaces this operator.

In this work, we present a new method of imaging the sea surface by using the decomposed upgoing and downgoing wavefields from a dual-sensor acquisition system. This is a method of direct sea-surface imaging in the sense that the reflection coefficients obtained thereof directly represent the sea-surface reflection operator of the seismic wavefield in contrast to methods based on swell noise inversion (e.g., Kragh et al., 2002).

METHODOLOGY

Wavefield separation and extrapolation

It is a well-known fact that recording seismic data by using collocated hydrophones and velocity sensors and properly combining the recorded wavefields, ghost reflections can be cancelled (Schneider et al., 1964; Claerbout, 1971, 1976). A collocated dual-sensor system simultaneously measures the pressure wavefield and vertical component of the particle velocity wavefield at a given acquisition depth. If the positive depth axis is pointing downward, the up- and downgoing wavefields are recorded with negative polarities for a velocity sensor but with respectively positive and negative polarities for a hydrophone. This is because of the negative reflection coefficient at the sea surface and the fact that the velocity sensor is directional whereas the hydrophone is a scalar sensor. In a homogenous medium, the pressure wavefield P and the vertical component of the particle velocity wavefield V_z are related as follows in frequency domain (Claerbout, 1971, 1976):

$$V_z = \frac{-dP}{i\rho\omega dz}, \tag{1}$$

where ρ represents the density, z defines the depth coordinate, and ω is the angular frequency. Thus, the relationship between the ghost functions of these two sensors (being 90° out-of-phase with each other as seen from equation 1) is exploited in data processing to decompose the measured seismic wavefields. For example, the upgoing and downgoing pressure wavefields in the frequency-wavenumber domain can be written in a matrix form as (plane-wave decomposition)

$$\begin{bmatrix} \tilde{U} \\ \tilde{D} \end{bmatrix} = \frac{1}{2} \begin{bmatrix} 1 & \frac{-\rho\omega}{k_z} \\ 1 & \frac{\rho\omega}{k_z} \end{bmatrix} \begin{bmatrix} \tilde{P} \\ \tilde{V}_z \end{bmatrix}, \tag{2}$$

where k_z is the vertical wavenumber and tilde designates the frequency-wavenumber transformed wavefields (e.g., Claerbout, 1976; Ursin, 1984; Amundsen, 1993). In equation 2, the streamer is assumed to be flat, which in reality is usually not the case. Fokkema and van den Berg (1993) show how similar equations can be derived for a smoothly shaped horizontal nonflat streamer. Application based on an implementation of these equations is presented in Söllner et al. (2008).

In the first step in imaging the sea surface, we extrapolate in small depth increments the separated upgoing wavefield and the downgoing wavefield upward toward the sea surface (Claerbout, 1976; Gazdag, 1978; Berkhout, 1982):

$$\tilde{U}(k_x,z_0,\omega) = \tilde{U}(k_x,z_R,\omega)\exp[ik_z(z_0 - z_R)], \tag{3}$$

$$\tilde{D}(k_x,z_0,\omega) = \tilde{D}(k_x,z_R,\omega)\exp[ik_z(z_R - z_0)]. \tag{4}$$

Equation 3 performs the extrapolation of the upgoing pressure wavefield from the data acquisition depth z_R (which is considered below the source depth level) to the sea-surface position z_0, which is assumed to be flat in this case. Also the scattered downgoing pressure wavefield, after muting the direct downgoing wavefield, is extrapolated upward toward the sea surface using equation 4. The upgoing wavefield is forward-propagated in time whereas the downgoing wavefield is backward-propagated in time.

Figure 1 shows that at the data acquisition depth, there is always a time delay between the measured upgoing and downgoing wavefields. As the separated wavefields are extrapolated toward the sea surface in a step-wise manner with a given step size, this delay time

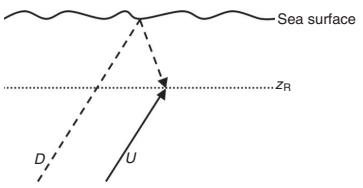

Figure 1. A sketch showing a rough sea surface, a streamer towed at a depth of z_R, and the upgoing (U) and downgoing (D) wavefields recorded by the sensor in the streamer.

becomes smaller. At the sea surface, the difference between the arrival times of the upgoing and downgoing wavefields is zero, as shown in Figure 2. One may view this extrapolation as bringing the streamer systematically closer and closer to the sea surface. Thus, when the streamer is exactly at the sea surface, the upgoing and downgoing wavefields are recorded exactly at the same time. For the flat sea surface, the amplitudes of upgoing and downgoing pressure wavefields cancel out after summation (Figure 2). This is because the downgoing wavefield is the same as the upgoing wavefield, except for a phase shift of 180° caused by the sea-surface reflection.

Imaging condition

After proper extrapolation of the decomposed monochromatic wavefields to the desired depth level, an estimate of the reflection coefficient(s) can be obtained by applying the classical *U*/*D* imaging condition and including all frequencies and sources available (Claerbout, 1971). However, this condition becomes unstable for small values of the downgoing wavefield. A stabilized version in which a stabilizing factor is added to the downgoing wavefield can be used (Vivas et al., 2009). Guitton et al. (2006) also show that the smoothing of the downgoing wavefield along the transversal coordinate can be used as a stabilizing criterion.

Alternatively, the least-squares imaging condition estimates the reflection coefficient by adding crosscorrelations of the upgoing and downgoing wavefields for all frequencies and sources available and dividing it by the total energy of the downgoing wavefield (Schleicher et al., 2008; Vivas et al., 2009). Many authors (among them are Vivas et al., 2009, Chattopadhyay and McMechan, 2008, and Schleicher et al., 2008) have shown that the least-squares imaging condition (also known as a source illumination map) is more robust and gives an improved image. Nevertheless, unconditional division by the autocorrelation can cause instabilities.

In the second step of sea-surface imaging, we apply an adequately adapted imaging condition that is a form of the least-squares imaging condition (Schleicher et al., 2008; Vivas et al., 2009)

$$I(x,z) = \frac{\sum_{\omega} U(x,z,\omega)\overline{D(x,z,\omega)}}{\sum_{\omega} U(x,z,\omega)\overline{U(x,z,\omega)}}, \qquad (5)$$

where the bar indicates conjugation. In a chosen time window of traces/channels, crosscorrelation of the extrapolated upgoing and downgoing wavefields is applied. The illuminating field in this case is the upgoing wavefield; here, the wavefields are extrapolated upward to the sea surface as opposed to the downward extrapolation used in migration in the case of subsurface reflectors. For each extrapolation step, the zero-lag amplitude values output from the crosscorrelations are divided by the zero-lag amplitude values output from the autocorrelations for each extrapolation step. Thus, by dividing with the zero-lag values of the autocorrelation, possible instability that would have been caused by a division with small values is avoided. The extrapolation depth associated with the maximum image value $I(x,z)$ for a given channel corresponds to the sea-surface elevation z at this channel position x. A plot of these extrapolation depths versus channel positions gives a time stationary image of the sea surface along the streamer corresponding to the selected time window. A sea-surface image at a different time is obtained by applying the imaging in a sliding time window mode.

It is pertinent to note that scattered waves comprising coherent and incoherent components arise when a sound wave is incident on a rough sea surface (e.g., Brekhovskikh and Lysanov, 2003). In this case, only the coherent component wavefield propagating in the direction of the specular reflection contributes to the image, and the obtained reflection coefficient is consequently less than unity.

SYNTHETIC DATA EXAMPLES

Ray-tracing approach

The proposed technique of sea-surface imaging was investigated using synthetic data based on dynamic ray tracing as well as time-domain finite-difference methods. First, a simple 2D acoustic plane layer model was constructed. The assigned layer velocities and densities are $V_P = 333$ m/s, $\rho = 0.01$ g/cm^3 (air); $V_P = 1500$ m/s, $\rho = 1$ g/cm^3 (water); and $V_P = 2500$ m/s, $\rho = 2$ g/cm^3 (sediment). In the modeling, a 40-m air layer and 200-m water layer were used. A source generating a typical airgun signature was placed at a depth of 6 m and towed at a distance of 50 m behind the vessel. The streamer was positioned at a depth of 15 m and 200 m behind the source.

A shot gather was generated for the hydrophone and velocity sensor by dynamic ray tracing. The wavefield separation was performed using equation 2. In a 400-ms time window of traces, the imaging condition was applied to the decomposed upgoing and downgoing pressure wavefields after extrapolating them to the sea surface. The optimal length of the imaging time window should be tested in each case and was chosen to be 400 ms here. The time-invariant flat sea-surface image obtained is used as a control reference. Figure 3 shows a plot of the estimated reflection coefficients for the same extrapolation depth superimposed on the theoretical reflection coefficients obtained using the Zoeppritz equation. Except for the first 10 channels, which are affected by edge effects, the estimated values are seen to have an average error of approximately 0.55%.

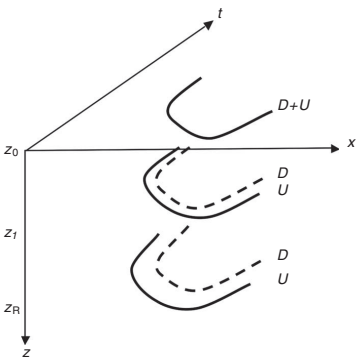

Figure 2. A sketch showing a step-wise extrapolation of the wavefields toward the sea surface. *U* is propagated forward in time whereas *D* is propagated backward in time. Amplitudes of the two wavefields sum to zero at the flat sea surface.

Sensitiveness of the imaging technique

To demonstrate the resolution limit of this technique, reflection coefficient estimates at different extrapolation depths (e.g., 1, 0.7, 0.6, …, 0.1 m) were obtained and plotted together with that of the actual (at 0.0 m) sea-surface reflection coefficient estimate. Figure 4 shows that the difference between the reflection coefficient estimates obtained for a 0.1-m extrapolation depth and that obtained for the true sea surface is very small. The average error for the reflection coefficient estimates for extrapolation depths of 0.1 m and the sea-surface extrapolation depths are 0.60% and 0.55%, respectively. Thus, deviations caused by sea-surface state (swell and other forms of noise) are solely resolvable if above 0.1 m. Nevertheless, the sensitiveness of this technique is hinged on the viability of the imaging technique and associated numerical implementations.

Error analysis

The reflection coefficient estimates obtained so far were from noise-free data. To carry out an error analysis of the imaging technique, random noise was superimposed on the generated synthetic data set having an amplitude value of 10% root mean square (rms) value of that of the noise-free data. The sea-surface image and the reflection coefficient estimates were obtained based on these data.

The noisy data gave the same good image of the sea surface as expected because the phase timing of the imaging condition is robust with respect to noise. This is expected because the imaging technique is robust with respect to noise. However, the noise introduced random errors in the estimated reflection coefficients and increased the average error to 2.26% (Figure 5). Although the reflection coefficient estimates obtained are also affected by other errors attributable to data truncation and numerical implementation inaccuracies, the amplitude part of the imaging condition (e.g., reflection coefficient values) is shown to be sensitive to additive random noise. Comparing the average error of noise-free data and the average error of the noisy data, which are 0.55% and 2.26%, respectively, the imaging technique is shown to be robust with respect to random noise.

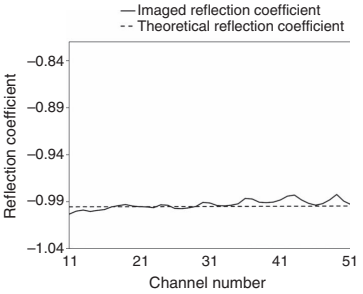

Figure 3. A plot of the maximum image point values for each channel.

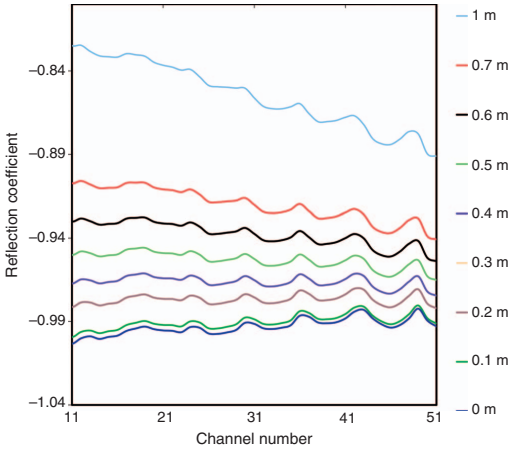

Figure 4. A plot of the image point values for each channel at various extrapolation depths. The vertical height between 0.1- and 0-m extrapolation depths compared to other extrapolation depths is very small.

Finite-difference approach

As a further demonstration of the robustness of this imaging technique, a finite-difference model in which the sea surface has a fairly realistic rough surface was used. A similar 2D acoustic model as in the previous example was used but with a spatially varying sea surface (Shepherd and McDonald, 2004). Hence, by superimposing three different sine waves corresponding to wavelengths of 0.9, 1.0, and 1.1 times the dominant wavelength of 120 m, a composite stationary sea-surface shape was simulated as shown in Figure 6. On the basis of the Beaufort scale and the World Meterological Organization sea state code, which classified a sea with significant wave height (SWH) of 2.5–4 m as a rough sea, we chose our SWH to be 4 m. Thus, the rough sea has a significant peak-to-peak wave height of 2 m around the sea-surface reference (40 m) depth level. Also, vacuum was used instead of air to make the sea surface a free interface. The other layer parameters were kept the same as in the previous model. The source was now placed in the center of the streamer spread to avoid edge effects and possible aliasing based on our survey layout. A Ricker wavelet with a center frequency of 60 Hz was used as the source signature. The model was gridded in both directions with a grid size of 60 cm.

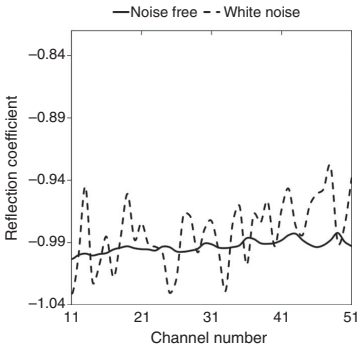

Figure 5. Plot of the maximum image point values for each channel for noise-free data and data-superimposed white noise corresponding to a 10% rms amplitude value of that of the noise-free data.

Figure 7 shows a close-up (see box in Figure 6) of parts of the modeled rough sea surface to be imaged. A plot of the upgoing and downgoing pressure wavefields from this area shows that, as expected, only the downgoing wavefield (receiver ghost) and other type of surface-related multiples carry information about the sea-surface condition as shown in Figure 8. Notice that the ripples observed on the ghosted primary (Figure 8a) are absent on the corresponding event in the upgoing wavefield (Figure 8b). On the other hand, small amplitude variations in the first surface-related multiple are still observable in the upgoing wavefield. This is because the upgoing primary reflected wavefield reflects from the flat seafloor whereas the downgoing wavefield and the multiples are also reflected from the sea surface after being reflected from the flat seafloor.

We applied our sea-surface imaging technique to the data of the selected area shown in the close-up picture. Here, a 400-ms time window was also chosen. The imaged sea-surface output for this area is plotted together with the extracted modeled sea surface as shown in Figure 9 and a very good match was obtained. The differences are mainly explained by the resolution limitation caused by using a 60-Hz Ricker wavelet.

FIELD DATA EXAMPLE

The field data were acquired by Petroleum Geo-Services (PGS) in the North Sea under marginal weather conditions, between 4-m swell height at the start of line and 2-m swell height at end of line, using a dual-sensor streamer that was towed at 15-m depth whereas the source array was towed at 7-m depth. Figure 10a-c shows the total pressure wavefield (Figure 10a), the upgoing (Figure 10b), and the downgoing pressure wavefields (Figure 10c) at the acquisition depth. The upgoing and downgoing wavefields were extrapolated to the acquisition datum level and summed together (Figure 10d). Observe that most of the amplitudes of the pressure field at 0-m extrapolation depth canceled out after adding the upgoing and downgoing wavefields. However, because the sea surface is not flat, residual amplitude values of the total wavefield are expected.

The first sea-surface image (Figure 11) was obtained after applying a 30-Hz high-pass filter with ramp from 20 Hz to the preprocessed field data. The filter was applied to remove that part of the data for which the vertical velocity field was contaminated by mechanical noise. The imaged result is considered a "frozen" (time-invariant) image of the sea surface corresponding to the time of the analysis window used (in this case 400 ms, starting from 200 ms of the field data).

Until now, only a time-invariant sea surface has been considered. For the time-varying sea-surface image, there is always a conflict regarding the choice of the length of the imaging time window. The design time window needs to be short so that the wavelet does not

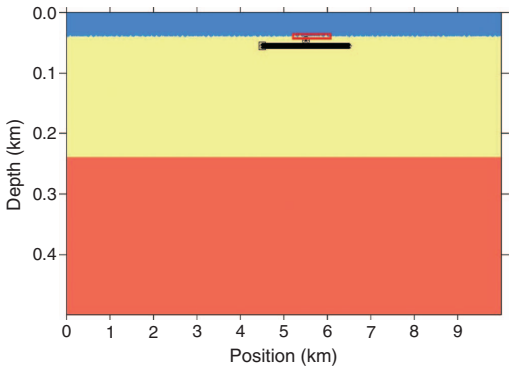

Figure 6. The 2D earth model showing the centered source and receiver layout, the sea surface, and seafloor. The inset (red box) shows part of the rough sea to be imaged.

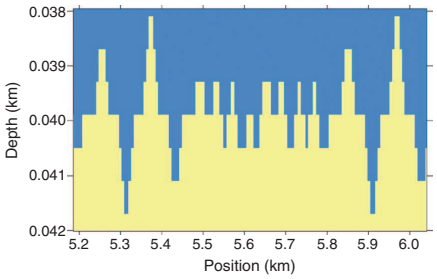

Figure 7. A close-up of the inset in Figure 6 showing part of the modeled rough sea surface to be imaged.

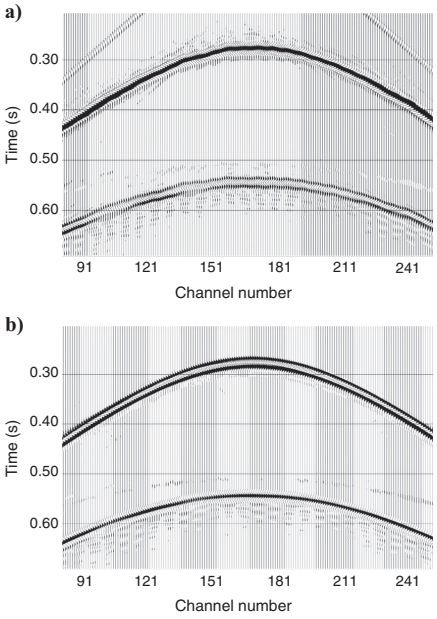

Figure 8. A common shot gather of the generated synthetic data for the rough sea surface demonstrating that only the downgoing wavefield (a) and the surface-related multiples carry information about the sea-surface state. The primary reflection of the upgoing wavefield in panel (b) is reflected from the flat seafloor, whereas the downgoing wavefield and the multiples are also reflected from the rough sea. The surface-related multiple, the second reflection event in the downgoing wavefield (a), is reflected twice at the sea surface, whereas the corresponding event in the upgoing wavefield (b) is reflected only once at the sea surface.

change too much, but it also needs to be long enough to capture the reflection event. A window length of 400 ms was also found to be a good choice in this case. To capture the dynamic nature of the sea-surface image, this imaging technique was repeated through a total of 1.8 s of the shot record by sliding the imaging time window 100 ms each time down the data. Thus, a total of 18 time-invariant sea-surface images at different times were obtained and these were plotted together and interpolated linearly as shown in Figure 12.

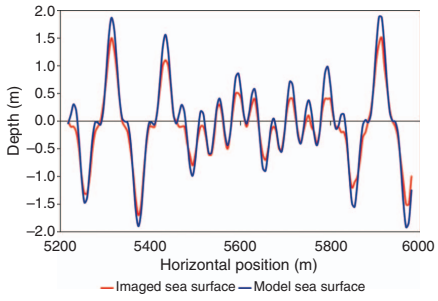

Figure 9. A plot of the true sea surface from the model in Figure 7 superimposed on the imaged sea surface. The difference between the modeled sea surface and imaged sea surface is mainly explained by the resolution limitation caused by using a 60-Hz Ricker wavelet as a source signature.

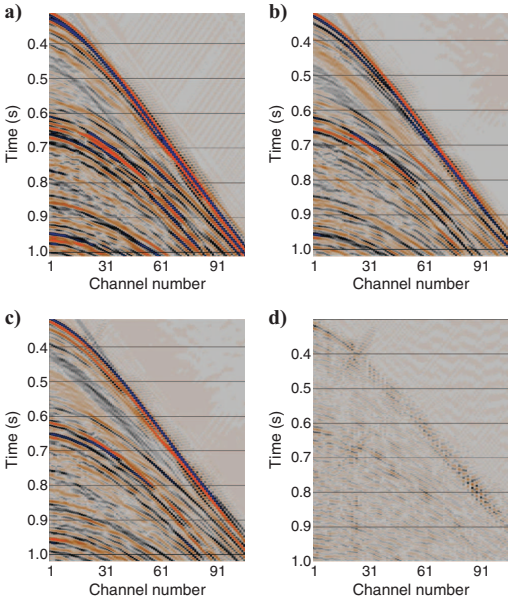

Figure 10. A common shot gather of (a) the total pressure wavefield, (b) the upgoing wavefield, and (c) the downgoing wavefield after wavefield separation of the field data at the acquisition depth. Figure 10d shows a common shot gather of the upgoing and downgoing wavefield summed at the acquisition datum level. Amplitude residue confirms that the sea surface was not flat at the time of data acquisition.

Imaging a time-invariant sea-surface shape has been demonstrated for a given time instant. Moreover, by placing such time-invariant sea-surface shapes side by side in a sequence, a time-variant sea-surface behavior could be obtained. In general, sea-surface shape variations are temporally and spatially irregular. The rising and falling of the sea-surface waves as they move toward higher channel numbers and as time elapses are observed in Figure 12. In particular, the peak observed at channel 38 apparently has moved to channel 41 (marked with broken line in Figure 13) within 1.8 s, corresponding to a water wave apparent speed of approximately 22.0 m/s, which represents a realistic value. However, given the limited data window imaged, the real behavior of the moving sea-surface wave is difficult to be captured solely from these sea-surface images (Figures 12 and 13).

Many factors contribute to the erratic behavior of the sea-surface wave. Wind speed and direction, water depth, land mass topography of the data acquisition area, and different artificial noise caused by man or sea life contribute to make the temporal behavior of the sea-surface shape very complicated. Nevertheless, the imaged result of the field data shows relatively smooth temporal and spatial variations. It is a common practice to stop seismic data acquisition in severe weather conditions (rough sea conditions of ≥ 4 m SWH). The imaged result from the field data has a SWH >2 m as shown. Thus, the estimated temporal and spatial variations of the sea-surface shape as shown seem reasonable.

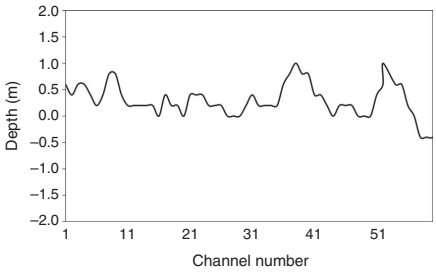

Figure 11. A plot showing a time-invariant sea-surface image obtained from the first time window of the field data.

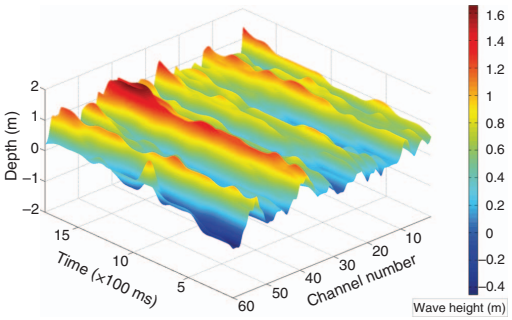

Figure 12. An interpolated plot of various time-invariant sea-surface images corresponding to different time windows simulating a time-variant sea-surface image.

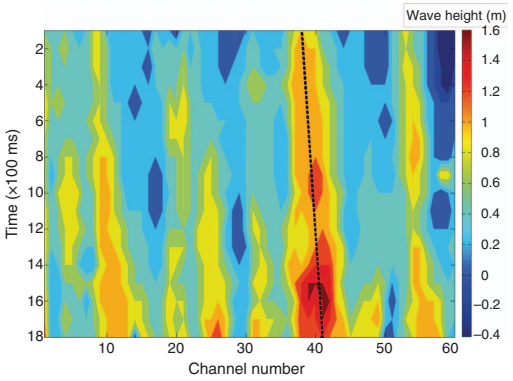

Figure 13. 2D contour plot showing temporal and spatial variations of the sea-surface waves. The broken line gives an apparent sea-surface wave speed of 22 m/s, assuming that the wave was moving along the streamer.

CONCLUSIONS

It is possible to image the shape of the sea surface using the upgoing and downgoing wavefields from dual-sensor towed streamer data. The scattered decomposed wavefields within a selected time window are extrapolated stepwise from the receiver level upward in the water layer. At every extrapolation step an adequate imaging condition is applied to image the water-air interface. Selecting a different time window gives a sea-surface image at a different time instant. Finally, using a sliding window through the data, the time-variable sea-surface condition was obtained.

This method was tested using synthetic data corresponding to a static rough sea surface and was also applied to field data acquired in the North Sea under marginal weather conditions. The imaged sea surface using the synthetic data sets correlates well with the corresponding true sea surface. The SWH during the acquisition of the field data was reported to be between 2 and 4 m and is in agreement with the SWHs obtained using our imaging technique.

A more elaborate test of the imaging technique using synthetic and field data will be carried out in the future. The discrepancy between the estimated reflection coefficients and the theoretical reflection coefficients will be investigated further, and the development of more robust estimators (imaging conditions) will be a prioritized task. To increase the reflection coefficient accuracy, the imaging condition will be applied in a plane-wave domain. Shot records will be analyzed to extract statistical properties of rough sea surfaces.

A good control of the frequency content of the signal and the corresponding frequency dependence of the resultant reflection coefficient estimates was possible in the synthetic data case because the medium was assumed to be nonviscous. However, this is not the case for the field data and will be addressed in future work.

Also, to further study the ability of the method to give accurate images of time-variant sea-surface conditions and reflection coefficient estimates, software able to generate controlled data associated with a moving sea surface should be developed. Future use of the imaging strategy discussed here can be to further refine seismic inversion and multiple elimination schemes. One of the crucial parts of dual-sensor processing is to recover the low-frequency part of the velocity sensor from the actual hydrophone measurements. This is carried out using a low-frequency condition assuming a flat sea surface and an ideal reflection coefficient of -1. In the future, one may foresee the development of iterative techniques able to update the low-frequency condition on the basis of the knowledge of the sea-surface state and corresponding reflection coefficient estimates.

ACKNOWLEDGMENTS

We are grateful to the Department of Geosciences at the University of Oslo for academic and financial support. We are grateful to PGS for permission to publish this work.

REFERENCES

Amundsen, L., 1993, Wave-number-based filtering of marine point source data: Geophysics, **58**, 1335–1348, doi: 10.1190/1.1443516.
Amundsen, L., 2001, Elimination of free-surface related multiples without need of the source wavelet: Geophysics, **66**, 327–341, doi: 10.1190/1.1444912.
Amundsen, L., T. Røsten, J. O. A. Robertsson, and E. Kragh, 2005, Rough-sea deghosting of streamer seismic data using pressure gradient approximations: Geophysics, **70**, no. 1, V1–V9, doi: 10.1190/1.1852892.
Berkhout, A. J., 1982, Seismic migration: imaging of acoustic energy by wavefield extrapolation: Elsevier Science Publishers.
Berkhout, A. J., and D. J. Verschuur, 1997, Estimation of multiple scattering by iterative inversion. Part I: Theoretical considerations: Geophysics, **62**, 1586–1611, doi: 10.1190/1.1444261.
Berkhout, A. J., D. J. Verschuur, and G. Blacquière, 2009, Seismic imaging with incoherent wavefields: 79th Annual International Meeting, SEG, Expanded Abstract, 2894.
Brekhovskikh, L. M., and Y. P. Lysanov, 2003, Fundamentals of ocean acoustics, 3rd ed.: Springer-Verlag.
Carlson, D., A. Long, W. Söllner, H. Tabti, R. Tenghamn, and N. Lunde, 2007, Increased resolution and penetration from a towed dual-sensor streamer: First Break, **25**, 71–77.
Carvalho, P. M., A. B. Weglein, and R. H. Stolt, 1991, Examples of a nonlinear inversion method based on the T matrix of scattering theory: application to multiple suppression: 61st Annual International Meeting, SEG, Expanded Abstracts, 1319–1322.
Chattopadhyay, S., and G. A. McMechan, 2008, Imaging conditions for prestack reverse-time migration: Geophysics, **73**, no. 3, S81–S89, doi: 10.1190/1.2903822.
Claerbout, J. F., 1971, Toward a unified theory of reflector mapping: Geophysics, **36**, 467–481.
Claerbout, J. F., 1976, Fundamentals of geophysical data processing: McGraw-Hill.
Fokkema, J. T., and P. M. van den Berg, 1993, Seismic applications of acoustic reciprocity: Elsevier Science Publishers.
Frijlink, M. O., R. G. van Borselen, and W. Söllner, 2009, On the free surface assumption for marine data driven demultiple methods: 71st Conference and Exhibition, EAGE, Expanded Abstracts.
Gazdag, J., 1978, Wave-equation migration by phase shift: Geophysics, **43**, 1342–1351, doi: 10.1190/1.1440899.
Ghosh, S. K., 2000, Deconvolving the ghost effect of the water surface in marine seismics: Geophysics, **65**, 1831–1836, doi: 10.1190/1.1444866.
Goto, R., E. Kragh, R. Laws, W. G. Morgan, and R. Phillips, 2008, Source and receiver measurements and corrections for the effects of sea surface wave height: 78th Annual International Meeting, SEG, Expanded Abstracts, 60–64, doi: 10.1190/1.3054855.
Guitton, A., A. Valenciano, D. Bevc, and J. Claerbout, 2006, Robust illumination compensation for shot-profile migration: 8th EAEG Meeting, Extended Abstracts, P265.
Ikelle, L. T., L. Amundsen, A. Gangi, and S. B. Wyatt, 2003, Kirchhoff scattering series: Insight into the multiple attenuation method: Geophysics, **68**, 16–28, doi: 10.1190/1.1543191.
Kragh, E., and R. Laws, 2001, Rough seas and statistical deghosting: 63rd Annual International Meeting, EAGE, Extended Abstracts, A022.
Kragh, E., R. Laws, and L. Combee, 2002, Sea surface shape derivation above the seismic streamer: 64th Meeting, EAGE, Expanded Abstracts, A007.
Laws, R., and E. Kragh, 2002, Rough seas and time-lapse seismic: Geophysical Prospecting, **50**, no. 2, 195–208, doi: 10.1046/j.1365-2478.2002.00311.x.
Robertsson, J. O. A., and E. Kragh, 2002, Rough sea deghosting using a single streamer and a pressure gradient approximation: Geophysics, **67**, 2005–2011, doi: 10.1190/1.1527100.
Schleicher, J., J. Costa, and A. Novais, 2008, A comparison of imaging con-

ditions for wave-equation shot-profile migration: Geophysics, **73**, no. 6, S219–S227, doi: 10.1190/1.2976776.
Schneider, A. W., K. L. Larner, J. P. Burg, and M. M. Backus, 1964, A new data-processing technique for the elimination of ghost arrivals on reflection seismograms: Geophysics, **29**, 783–805.
Shepherd, A. M., and J. A. McDonald, 2004, Quantification of swell noise on seismic lines gathered in rough and calm seas: EAGE 66th Conference, H023.
Söllner, W., E. Brox, M. Widmaier, and S. Vaage, 2007, Surface related multiple suppression in dual sensor towed streamer data: 77th Annual International Meeting, SEG, Expanded Abstracts, 2540–2544.
Söllner, W., A. Day, and H. Tabti, 2008, Space-frequency domain processing of irregular dual-sensor towed streamer data: 78th Annual International Meeting, SEG, Expanded Abstracts, 1078–1082.
Tenghamn, R., S. Vaage, and C. Borresen, 2007, A dual-sensor, towed marine streamer; its viable implementation and initial results: 77th Annual International Meeting, SEG, Expanded Abstracts, 989–993.
Ursin, B., 1984, Seismic migration using the WKB approximation: Geophysical Journal of the Royal Astronomical Society, **79**, 339–352.
van Borselen, R. G., J. T. Fokkema, and P. M. van den Berg, 1996, Removal of surface-related wave phenomena — The marine case: Geophysics, **61**, 202–210, doi: 10.1190/1.1443940.
Verschuur, D. J., 1991, Surface-related multiple elimination, an inversion approach: Ph.D. thesis, Delft University of Technology.
Vivas, A. F., R. C. Pestana, and B. Ursin, 2009, A new stabilized least-squares imaging condition: Journal of Geophysics and Engineering, **6**, no. 3, 264–268, doi: 10.1088/1742-2132/6/3/005.

Paper II

Effects of time-varying sea surface in marine seismic data

Orji O. C., W. Söllner and L-J. Gelius

Geophysics **77**, P33-P43

GEOPHYSICS, VOL. 77, NO. 3 (MAY-JUNE 2012); P. P33–P43, 13 FIGS.
10.1190/GEO2011-0361.1

Effects of time-varying sea surface in marine seismic data

Okwudili C. Orji[1], Walter Söllner[2], and Leiv-J. Gelius[3]

ABSTRACT

A method of imaging sea surfaces based on marine seismic measurements has recently been developed. The imaging technique is based on extrapolating decomposed wavefields obtained from dual-sensor streamers to the sea surface where an adequate imaging condition is applied. Earlier feasibility tests of the method involved only controlled data associated with frozen sea surfaces. Here, the issue of time-varying effects will be in focus. We introduced a modeling approach based on the Kirchhoff-Helmholtz integral and computed the scattered wavefield from time-varying rough sea surfaces (e.g., Pierson-Moskowitz sea surfaces). We generated data for a realistic wind speed and verify the robustness of the proposed sea surface imaging technique by taking into account possible effects of moving receivers as well as streamers with variable shape. We investigate the feasibility of estimating the surface wave velocity from the spectra of the imaged sea surfaces and finally present a successful application of the sea surface imaging technique to data from the North Sea.

INTRODUCTION

Sea surface topography is a subject of wide interest in the scientific community. In remote sensing, directional information of ocean surface waves is obtained from synthetic aperture radar (SAR). Many authors have investigated ocean surface SAR images among them are Schulz-Stellenfleth and Lehner (2001), Hasselmann and Hasselmann (1991), and Alpers et al. (1983). Schulz-Stellenfleth et al. (2001) used across-track interferometric synthetic aperture radar (InSAR), but obtained distorted digital elevation models of the sea surface because of the continuous motion of the sea wave. The observed distortions were dependent on the amplitude of the ocean swell.

In underwater acoustics, scattering of acoustic waves by the sea surface has been studied extensively. The nature and time variable changes of the sea surface are important factors considered in submarine warfare and fish finding (e.g., Clay and Medwin, 1977; Urick, 1983), as well as acoustic underwater communications (e.g., Stojanovic, 1996). In many sonar applications, solutions of the ocean acoustic scattering problems are often formulated in the frequency-domain implying a "frozen" sea surface in time (e.g., Siderius and Porter, 2008). Considering the frequency band typical for acoustic communications (e.g., 1–50 kHz), the effects of a moving source, moving receiver and a moving sea surface cannot be neglected.

If not taken care of properly, reflections from the sea surface degrade the seismic image. High-resolution images are essential for quantitative seismic interpretation and improved reservoir monitoring. Laws and Kragh (2002) discuss effects of rough sea surface scattering on 4D seismic data. In time-lapse seismic, where successive seismic images of producing field aids geophysicists in identifying bypassed oil, the destructive effects of the sea surface prove to be a challenge when the successive images are matched. This is because the sea surface conditions vary continuously. However, various seismic processing and imaging methods that actively make use of sea surface reflections, assume flat and stationary sea surface conditions and consequently a reflection coefficient of -1.

Thus, there is a need for techniques that can describe the time-varying effects of the sea surface. A large literature exists on scattering of sound by rough surfaces. Modeling of scattered wavefields from rough sea surfaces based on the Helmholtz integral (Holford, 1981) or the Helmholtz integral with the Kirchhoff approximation included have been used by many authors. Thorsos (1988, 1990) and coworkers discuss scattering from Gaussian and Pierson-Moskowitz surfaces. Siderius and Porter (2008) discuss broadband ocean acoustic transmissions associated with a time-varying sea surface. Laws and Kragh (2002) investigate scattering from rough time-varying sea surfaces using the Kirchhoff method

Manuscript received by the Editor 27 September 2011; revised manuscript received 22 December 2011; published online 20 April 2012.
[1]University of Oslo, Department of Geosciences, Norway; Petroleum Geo-Services, Oslo, Norway. E-mail: okwudilo@student.geo.uio.no.
[2]Petroleum Geo-Services, Oslo, Norway. E-mail: walter.sollner@pgs.com.
[3]University of Oslo, Department of Geosciences, Norway. E-mail: l.j.gelius@geo.uio.no.

and a specialized finite difference (FD) method. They simulate this time-variation by employing different realisations of the Pierson-Moskowitz sea surface for separate shot records and phase-rolling for short time wavelet variations. Orji et al. (2010) presented a method of imaging sea surfaces based on dual-sensor data. In this method, the scattered wavefields from the subsurface were separated from the receiver ghosts and both wavefields were subsequently extrapolated upward in small depth steps to the sea surface and an imaging condition was applied. They investigated the accuracy of the proposed technique by computing scattered data from frozen sea surfaces based on dynamic ray tracing and acoustic finite-difference methods. To the knowledge of the authors no attempts of imaging a time-varying sea surface based on modeled data have been reported in the literature.

This paper can be considered a continuation of the previous work of Orji et al. (2010), but this time a forward modeling tool based on the Kirchhoff-Helmholtz integral is developed. It can handle time-varying Pierson-Moskowitz sea surfaces, moving receivers as well as a streamer with a variable shape. Thus, the marine seismic experiment can be modeled in a more realistic manner. Such controlled data can then be used to demonstrate the robustness of the sea surface imaging technique introduced by Orji et al. (2010) with respect to time-varying effects. When imaging the modeled sea surface we use a variable depth wavefield separation technique that takes into account the true depth of each of the sensors along the streamer as opposed to using a nominal depth. The analyses also include possible effects of moving receivers. Moreover, by use of a spectral analysis of the sea surface the feasibility of estimating the surface-wave velocity is demonstrated. Finally, a successful application of the method to a North Sea data set is presented.

METHODOLOGY

Collocated dual-sensor streamer systems simultaneously measure normal particle velocity and pressure wavefields (e.g., Tenghamn et al., 2007). A correct combination of these wavefields yield upgoing and downgoing pressure or velocity wavefields (e.g., Schneider et al., 1964; Claerbout, 1971, 1976; Amundsen, 1993; Carlson et al., 2007). A method of using the separated wavefields to image the sea surface has been described by Orji et al. (2010). In summary, the separated upgoing and downgoing pressure or velocity wavefields are extrapolated in small steps toward the sea surface where an adequate imaging condition is applied. The depth positions of the maximum image point values define the sea surface. By using a sliding window through the data and repeating the imaging technique for each window, the time variable changes of the sea surface can be accounted for.

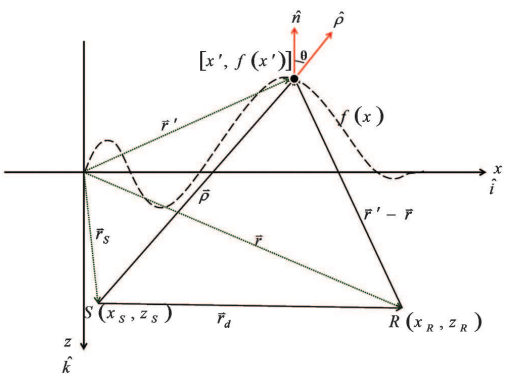

Figure 1. A sketch showing the coordinates of the source S, the receiver R, and the running scattering point $[x', f(x')]$ on the sea surface $f(x)$.

Kirchhoff-Helmholtz integral modeling formulation (frequency domain)

This work starts with the 2D Kirchhoff-Helmholtz integral equation (monochromatic steady-state waves in a homogeneous half-space) describing wave scattering from a 1D rough sea surface with the free-surface boundary condition imposed (see equation 1 and Figure 1):

$$P(\vec{r},\omega) = \frac{1}{4i}H_0^{(1)}(k|\vec{r}_d|)S(\omega) - \frac{1}{4i}\int_{\partial L}[H_0^{(1)}(k|\vec{r}\,' - \vec{r}|)]\frac{\partial P(\vec{r}\,',\omega)}{\partial n'}dl', \quad (1)$$

where $H_0^{(1)}$ is the zeroth-order Hankel function of the first kind, $S(\omega)$ is the source spectrum, k is the wavenumber of the propagating wavefield and dl' is the length parameter along the rough surface (e.g., Holford, 1981; Thorsos, 1988, 1990; Amundsen, 1994; Siderius and Porter, 2008). The first term on the right-hand side of equation 1 is the incident field ($P_{inc}(\vec{r},\omega)$), whereas the second term represents the scattered waves. To establish the notation being used here, the following quantities are introduced with reference to Figure 1:

$f(x)$ represents the surface height function; $[x', f(x')]$ defines the position of a scattering point on the surface; $\vec{r}$ defines a vector from the origin to the running scattering point; $\vec{r}\,'$ defines a vector from the origin to a fixed receiver position; $\vec{r}\,' - \vec{r}$ is a vector from a given receiver position to the running scattering point; $\vec{r}_d$ is a vector from a source position to the receiver; $\vec{r}_s$ defines a vector from the origin to the fixed source position; $\vec{\rho}$ defines the vector from the fixed source position to the running scattering point; the unit vectors $\hat{n}$ and $\hat{\rho}$, respectively denote the normal to the surface and the unit vector direction of the incident field at $[x', f(x')]$; the obliquity factor is given by $\cos\theta = \hat{n}\cdot\hat{\rho} \equiv \eta(x')$ (see Figure 1).

Exact method

The solution to scattering from a rough surface with a free boundary condition is given by equation 1. The unknown normal derivatives of the pressure field on the rough surface, $\frac{\partial P(\vec{r}\,',\omega)}{\partial n'}$, can be obtained from the following equation by considering receiver points placed along the sea surface and assuming a boundary condition of zero total pressure field at the rough surface:

$$P_{inc}(\vec{r},\omega) = \frac{1}{4i}\int_{\partial L}[H_0^{(1)}(k|\vec{r}\,' - \vec{r}|)]\frac{\partial P(\vec{r}\,',\omega)}{\partial n'}dl'. \quad (2)$$

Equation 2 is a Fredholm integral equation of the first kind which is solved using numerical inversion to give the wavefield gradient,

$\frac{\partial P(\vec{r},\omega)}{\partial n}$, (e.g., Holford, 1981; Thorsos, 1988; Siderius and Porter, 2008). By combining this result with equation 1, the total field at a given receiver can be computed. In this paper, this two-step method is denoted the "Helmholtz Exact" (HE) approach. The exact method (HE) as outlined here serves as a reference and will be used as a quality control for the approximate method.

Kirchhoff approximation

The computational time of the exact method can be prohibitively large especially when a time-varying surface is considered. In contrast, the Kirchhoff approximation is known to be much faster, and due to the low-frequency characteristic of the rough surface considered here, it is expected to work quite well. The underlying assumptions of the Kirchhoff approximation are that the sea surface is locally planar on the scale of the dominating wavelength of the wavefield or alternatively that the radius of curvature of the sea surface is large compared with the dominating seismic wavelength. Assuming a pressure release surface and imposing continuity and energy conservation, the Kirchhoff approximation can be described by the following condition (Meecham, 1956; Thorsos, 1988):

$$\frac{\partial P(\vec{r},\omega)}{\partial n} \cong \frac{2\partial P_{inc}(\vec{r},\omega)}{\partial n}. \tag{3}$$

Combining equations 1 and 3 and representing the incident field by a line source gives the Helmholtz-Kirchhoff (HK) equation (see appendix A for details):

$$P(\vec{r},\omega) = \frac{1}{4i}H_0^{(1)}(k|\vec{r}_d|)S(\omega) + \frac{kS(\omega)}{8}\int_{\partial L} H_0^{(1)}(k|\vec{r}\,' - \vec{r}|) \times H_1^{(1)}(k|\vec{\rho}|)\eta(x')dx', \tag{4}$$

with

$$\eta(x') = \frac{-(x'-x_s)\frac{df(x)}{dx}\Big|_{x=x'}}{|\vec{\rho}|} + \frac{[f(x')-z_s]}{|\vec{\rho}|},$$

where $H_1^{(1)}$ is the first-order Hankel function of the first kind and $\eta(x')$ is the obliquity factor. The validity of this equation will be demonstrated employing HE as a reference for frozen sea surface conditions.

Kirchhoff-Helmholtz integral (time domain)

To model the time-varying changes of a sea surface properly, the time-domain version of the Kirchhoff-Helmholtz integral is needed. This is achieved by introducing the asymptotic form of the Hankel functions in the frequency-domain version of the Kirchhoff-Helmholtz integral (see equation 4). This suffices for larger values of the arguments of the Hankel functions (i.e., $k|\vec{r}| > 1$) because the separated upgoing and downgoing wavefields, which represent the inputs to the sea surface imaging algorithm, are usually in the far field region. The asymptotic forms of the Hankel functions present in equation 4 are given as (e.g., Watson, 1962; Abramowitz and Stegun, 1972; Arfken, 1985):

$$H_n^{(1)}(x) \cong \sqrt{\frac{2}{\pi x}}e^{i(x-\frac{\pi}{4}-\frac{n\pi}{2})}, \qquad n = 0, 1, 2, \ldots\ldots \tag{5}$$

By substituting equation 5 into equation 4 and applying an inverse Fourier Transform, the time-domain version of the Kirchhoff-Helmholtz integral is obtained (see appendix B):

$$P(\vec{r},t) = \frac{1}{2}\sqrt{\frac{c}{2\pi|\vec{r}_d|}}q(t-\tau_d) - \frac{1}{4\pi}\int_{\partial L}\frac{s(t-\tau(x'))}{\sqrt{|\vec{r}\,'-\vec{r}||\vec{\rho}|}}\eta(x')dx', \tag{6}$$

with

$$\tau = \tau_s + \tau_r = \frac{|\vec{\rho}|}{c} + \frac{|\vec{r}\,'-\vec{r}|}{c},$$

where τ_d is the traveltime of the direct wavefield, τ_s is the traveltime of the incident wavefield from the source to a scattering point on the sea surface, τ_r is the traveltime from the same scattering point to the receiver, c is the sound speed in water, and q represents a filtered version of the original source pulse as follows:

$$e^{-i\frac{3\pi}{4}}\frac{1}{\sqrt{\omega}}S(\omega)e^{i\omega\tau_d} \overset{IFT}{\rightarrow} q(t-\tau_d).$$

Finally, the effects of a time-varying sea surface are included by modifying equation 6 as follows: the surface height function must be allowed to vary with time and one has to introduce the proper time lag to account for causality, which implies that $\eta(x')$ is replaced by $\eta(x', t-\tau_r)$ in equation 6. This time-varying modeling approach will be denoted HKT. The 3D versions of equations 1, 2, and 6 are obtained by including the y' dimension of the running scattering point. However, in the validation tests presented here, 2D synthetic data will be employed to speed up the computations.

SYNTHETIC DATA GENERATION AND IMAGING

To determine the shape of the sea surface from the modeled data, wavefield separation is applied at the receiver level to decompose the data into the upgoing and downgoing components. After wavefield separation an imaging condition is applied to the extrapolated wavefields (e.g., Claerbout, 1976; Orji et al., 2010):

$$I(x,z_R) = \frac{\sum_\omega U(x,z_R,\omega)\overline{D(x,z_R,\omega)}}{\sum_\omega U(x,z_R,\omega)\overline{U(x,z_R,\omega)}}, \tag{7}$$

where z_R is the receiver depth, x is the receiver position, and ω is the angular frequency. U and D are, respectively, the upgoing and downgoing components of an arbitrary reflected or scattered wavefield from the subsurface. The above least-squares imaging condition is in general stable (e.g., Schleicher, 2008). Further stabilization, by adding a constant to the autocorrelation, did not yield better images because zero-lag values of the autocorrelation are always taken in the evaluation of the denominator thus, avoiding

possible instabilities. In generating the synthetic data, a split spread configuration was generally used. The upgoing wavefield was generated by placing one or several secondary sources below the receivers assuming a homogenous (water) half space. Correspondingly, the downgoing wavefield was formed when this wavefield was scattered from the rough sea surface.

The lateral dimension of the modeled sea surface was assumed 1023 m long and it was discretized with a spacing of $\Delta x = 3$ m, which gives a total of $N = 341$ running scattering points. In the examples shown here, a rather dense sampling of the sea surface was used to avoid numerical artifacts. It has been reported in the literature that at least a sampling density corresponding to $\lambda/5$ (with λ being the dominant wavelength) is required in practice (e.g., Thorsos, 1988, 1990). The water medium was assigned an acoustic speed of 1500 m/s and a density of 1000 kg/m^3. A free-surface boundary was assumed at the water surface.

Frozen rough sea surface (composite of three sinusoidal waveforms)

A spatially varying sea surface was modeled from a combination of three sine waves corresponding to wavelengths of 0.9, 1.0, and 1.1 times the dominant wavelength of 120 m. A Significant Wave Height (SWH) of 4 m (subjective peak-to-trough wave height) was used to simulate this composite time invariant sea surface. A 90 Hz Ricker wavelet source sampled at 1 ms was placed at a depth of 700 m directly below the middle receiver. A total of 101 receivers, separated by 6 m and placed at a depth of 50 m below the sea surface, were used.

Data were generated using the HE, HK, and HKT modeling approaches. Each data set was used as input to the imaging technique to give a reconstruction of the original sea surface (see Figure 2). Observe the good match between the true sea surface and each of the imaged sea surfaces. Nevertheless, some discrepancies still exist at the grooves of the image curves, which can be attributed to minor errors due to the numerical implementations.

Time-varying sea surfaces

The previous example demonstrated the accuracy of the Kirchhoff approximation for typical sea-surface wavelengths. Moreover, the use of asymptotic Hankel functions does not degrade the result in case of the time-domain approximations. Thus, HKT can be employed to model wavefield scattering from a given sea surface. Consider now the case of a time-varying sea surface. The Pierson-Moskowitz method was employed to define a realistic sea state.

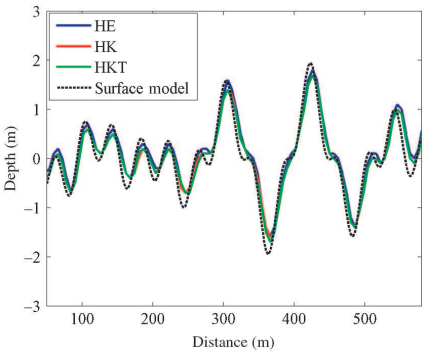

Figure 2. A plot of the true sea surface and the imaged sea surfaces for data generated based on HE, HK, and HKT.

Naturally, sea surface is a spatiotemporal dependent surface. The degree of the roughness is among other factors dependent on the prevailing wind speed. Beaufort Wind Force Scale classifies different sea surface states based on these speeds. As the wind speed increases, the roughness of the sea surface increases (i.e., the sea surface wavelength and wave height increases). The spectrum of such a sea surface is approximately described by the Pierson-Moskowitz sea surface spectrum for a fully developed sea (Pierson and Moskowitz, 1964; Neumann and Pierson, 1966; Pond and Pickard 1983; Thorsos, 1990; Laws and Kragh, 2002). The Pierson-Moskowitz spatial roughness spectrum in 1D is given as:

$$W(K) = \left[\frac{\alpha}{(4|K|^3)}\right] e^{-(\beta g^2)/(K^2 U_w^4)}, \tag{8}$$

where K is the sea surface-wave spatial wavenumber, U_w is the wind speed (measured at a height of 19 m), α and β are constants of, respectively, 8.10×10^{-3} and 0.74, while g is the acceleration due to gravity. A technique for generating 1D sea surface realizations is used assuming a random phase shift between each wavenumber component (Thorsos, 1988). The sea surface height function $f(x')$ is generated at the running scattering point x' as follows:

$$f(x') = \frac{1}{L}\sum_{j=0}^{N-1} F(K_j) e^{iK_j x'}, \tag{9}$$

where, for $j \geq 0$,

$$F(K_j) = [2\pi L W(K_j)]^{1/2} \begin{cases} [N(0,1) + iN(0,1)]/\sqrt{2}, j \neq 0, N/2 \\ N(0,1), j = 0, N/2 \end{cases} \tag{10}$$

and for $j < 0$, $F(K_j) = F(K_{-j})^*$. In equations 9 and 10, the spatial wavenumber for component j is given as $K_j = 2\pi j/L$ and L is the spatial length of the surface. The random number $N(0,1)$ is generated from a Gaussian distribution having zero mean and a unit variance. Thus, the sea surface is formed by adding each wavenumber component imposing random phase shifts. A frozen Pierson-Moskowitz sea surface can now be computed from equation 10 using fast Fourier transform.

Sea surface waves are dispersive and in deep water, frequency and wavenumber are related by this dispersion relation (e.g., Ishimaru, 1997):

$$\omega_j = \sqrt{g\frac{(2\pi j)}{L}}. \tag{11}$$

Equation 11 implies that each space harmonic component of the surface may move with a definite phase velocity. Thus, in general sea waves of longer wavelengths travel faster relative to shorter ones. By combining equations 10 and 11 a time-varying Pierson-Moskowitz sea surface is obtained as follows:

$$f(x',t) = \frac{1}{L}\sum_{j=0}^{N-1} F(K_j)e^{i(K_j x' - \omega_j t)}, \qquad (12)$$

where t is the instantaneous time at the running scattering point x'. Equation 12 describes a 1D rough sea surface moving in the positive x-direction.

The time-varying Pierson-Moskowitz sea surface was modeled based on equation 12 for a wind speed of 17 m/s. This wind speed was chosen after verifying through simulations that it corresponds to a moderately rough sea surface. To generate an upward traveling wavefield that mimics a subsurface scattered wavefield, 15 different sources were distributed laterally between 410 and 610 m and vertically between 700 and 1400 m and fired simultaneously. In the computations, a temporal sampling interval of 2 ms was employed and data was recorded for 1.6 s. The time variation of the sea surface is captured by applying the imaging technique in a sliding window mode. The window is 400 ms long and is slid 10 ms down the data each time.

Figure 3a and 3b shows surface plots of the true and the imaged sea surfaces obtained by interpolating linearly between sea surface profiles imaged at different times. Figure 4 shows a profile of the true and the imaged surfaces for one time instant. As can be seen from all figures and Figure 4 in particular, a good match exists between the true (modeled) and the imaged surfaces. However, parts of the modeled surface characterized by small wave heights were not well resolved; this can be attributed to the resolution limit of our 90 Hz source pulse.

Effect of moving receivers

The data used in the previous sections were computed assuming fixed receivers. In a real marine seismic experiment, once the source is fired, the receivers are in constant motion during data acquisition. In other words, the source can be assumed to be instantaneously stationary at the firing point while the receivers typically move with a velocity of about 2.5 m/s (approximately five knots) when recording the reflected seismic data. Thus, to study the additional effects of a moving receiver, each of the receivers in the previous section were made to move: first with a velocity of 2.5 m/s and then with an unrealistically high velocity of 7.5 m/s (14.5 knots) in the negative x-direction. Denote now a given receiver j by R_j and assume its initial coordinates are x_R and z_R (i.e., at time $t = 0$). If the receiver moves with a constant lateral velocity u, it will change to a new position $R_j(x_R + un\Delta t, z_R)$ after a time $t = n\Delta t$.

Thus, as the sea surface starts moving at each time step Δt, the receivers also start moving in the opposite direction with respect to the sea surface. Figure 5 shows a plot of the imaged sea surface profiles for the receiver velocities considered. As expected, the imaged sea surface (green line) obtained for receivers moving at a typical seismic vessel speed of 2.5 m/s matches the one obtained assuming stationary receivers (blue broken line). However, the sea surface profile (red line) obtained for receivers moving at a speed greater than a typical seismic vessel speed (7.5 m/s) shows a noticeable shift to the left (i.e., in the direction of the moving receivers) compared with the reference sea surface profile of stationary receivers (blue broken line). In conclusion, for a typical seismic survey, the effect of moving receivers is negligible and does not need to be accounted for during sea surface imaging. An unrealistically high vessel speed of 7.5 m/s was deliberately chosen to be able to visualize the effect of vessel speed on the imaged sea surface.

Geometrical effects

During a marine seismic data acquisition, the streamers are seldom flat. A combination of many factors including ocean swell, failure of depth control devices, accumulation of barnacles on

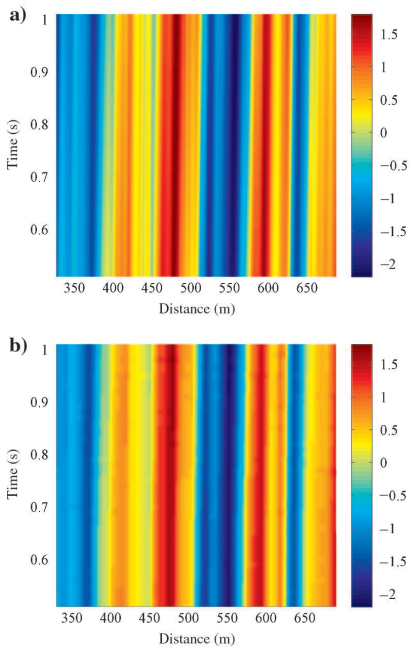

Figure 3. (a) Surface plot of the modeled time-varying Pierson-Moskowitz sea surface for a wind speed of 17 m/s. (b) Corresponding imaged sea surface.

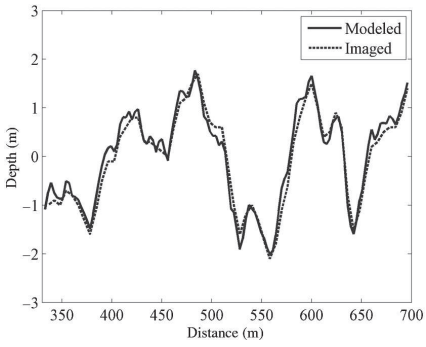

Figure 4. Modeled and imaged Pierson-Moskowitz sea surface profiles corresponding to a fixed observation time of 0.9 s.

the streamers etc., makes the receivers deviate from the nominal desired depth along the towed streamers. Depth control equipments such as birds are normally attached to the streamers to maintain a relatively constant depth during data acquisition. Nevertheless, because the birds are attached at certain intervals, typically 300 m along the streamer, the depth of the receivers along the towed streamers still varies. Thus, to simulate typical depth variations of the sensors during data acquisition we assumed that the depth of the receivers varied between 50.5 m and 49.5 m following a sinusoidal function with a 600 m wavelength (see Figure 6). In the simulations to be shown, the receivers were assumed stationary.

The variation in depth of the receivers can be corrected for, before imaging, by redatuming the acquired data based on variable depth wavefield separation. Fokkema and van den Berg (1993) demonstrated how variable depth wavefield separation can be performed. Numerically, this can be carried out based on equations 14 and 15 (Söllner et al., 2008).

Figure 6 shows a typical variable receiver depth profile used in the modeling (red curve) together with the corresponding nominal depth (blue line). Figure 7 shows the imaged sea surface profile (red line) for data generated with variable depth receivers but assuming a nominal receiver depth of 50 m during imaging. The blue and green lines, respectively, show the imaged sea surface profile for data generated with a flat streamer (reference) and data generated with variable receiver depth but where the true receiver depths are taken into consideration during the imaging process. In Figure 7, the blue line is completely overlaid by the green line implying a perfect match between the two. Thus, by considering Figures 6 and 7, it can be seen that the effect of using a nominal receiver depth during imaging instead of the correct receiver depths is a vertical displacement of the imaged surface. Thus, errors that can arise as a result of streamer depth variation can be avoided if the true receiver depths are taken into consideration in performing wavefield separation.

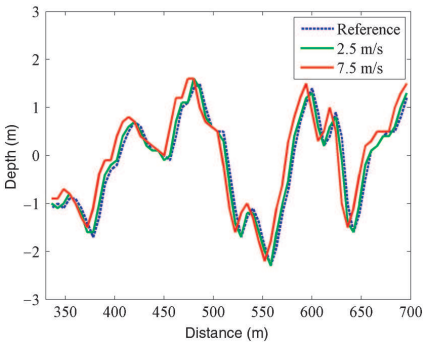

Figure 5. The green curve shows the imaged Pierson-Moskowitz sea surface profile for receivers moving at a speed of 2.5 m/s, the red curve shows the same in case of receivers moving at a speed of 7.5 m/s. Finally, the blue dotted curve shows the imaged sea surface profile for stationary receivers.

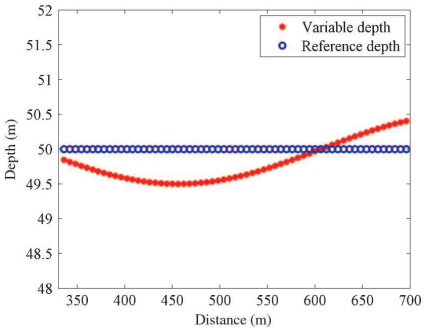

Figure 6. A plot of a typical variable receiver depth profile used in the modeling (red curve) together with the corresponding nominal depth (blue line).

Surface wave velocity estimation from spectral analysis

In this work, the Pierson-Moskowitz sea surface profile was obtained from the Pierson-Moskowitz frequency spectrum for a fully developed sea. The spatial roughness spectrum is in this case given by equation 9. The sea surface waves are dispersive by nature and this is reflected in the Pierson-Moskowitz spectrum. Assume now that the dominant wavelength travels at a speed close to the group velocity and therefore also close to that of the prevailing wind speed. For a given peak wavenumber K_{peak} the corresponding surface wave velocity can be calculated from the dispersion relation:

$$v_{peak} = \sqrt{g/K_{peak}}, \tag{13}$$

We will now use the modeled sea surface to test this hypothesis. An estimate of the Pierson-Moskowitz spectrum can now be calculated by taking the spatial Fourier transform of these modeled sea surfaces for each observation time and taking the average (to avoid end effects a Tukey window is applied [see Figure 8]). The lateral dimension of the sea surface was set to 1023 m. By picking the

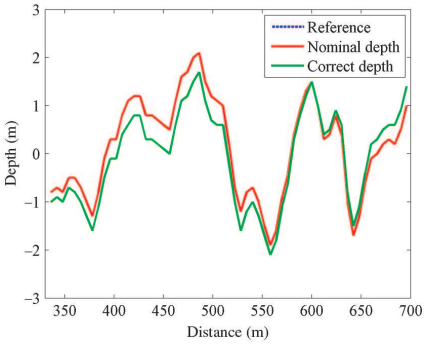

Figure 7. The red curve shows the imaged Pierson-Moskowitz sea surface profile with variable depth receivers not accounted for during imaging. The blue broken curve shows the imaged sea surface profile obtained with receivers at the same depth (flat streamer) and the green curve shows the imaged sea surface profile obtained in case of receivers with variable depth where these variations are accounted for during imaging. (Note the green and blue curves completely superimpose each other).

largest wavenumber value in the spectrum and making use of equation 13, an estimate of the velocity with which the dominating wavelength is traveling can be obtained. The estimated velocity was found to be about 17 m/s which fits well with the prevailing wind speed of 17 m/s originally assumed. Note, however, the accuracy of such a spectral method relies on a sufficient length of the sea surface covered by the measurements. Use of a short measurement window will introduce ambiguity. Note also that this demonstration has been carried out using an analytical sea surface description. In the next section the same analysis will be carried out employing field data.

FIELD DATA EXAMPLE

The field data was acquired by PGS in the North Sea under marginal weather conditions with about 4 m swell height at the start of the line and 2 m swell height at end of the line. A dual-sensor streamer was towed at a nominal depth of 15 m depth while the source array was towed at 7 m depth. The field data was preprocessed and wavefield separation was performed. In Orji et al. (2010), the nominal depth of the receivers were used when performing the wavefield separation as opposed to taking the actual depth variation along the streamers into account. In this paper, based on the work of Fokkema and van den Berg (1993) a variable depth wavefield separation is employed. Numerically this can be performed based on the following equations (Söllner et al., 2008):

$$P^{up}(n\Delta k_x,\omega)=\frac{\Delta x}{-2ik_z}\sum_m\{i\omega\rho V_{\vec{n}}(x_R^m,z_R^m,\omega)\exp[in\Delta k_x x_R^m-ik_z z_R^m]+P(x_R^m,z_R^m,\omega)\exp[in\Delta k_x x_R^m-ik_z z_R^m][in\Delta k_x n_x-ik_z n_z]\},\quad(14)$$

$$P^{down}(n\Delta k_x,\omega)=\frac{\Delta x}{2ik_z}\sum_m\{i\omega\rho V_{\vec{n}}(x_R^m,z_R^m,\omega)\exp[in\Delta k_x x_R^m+ik_z z_R^m]+P(x_R^m,z_R^m,\omega)\exp[in\Delta k_x x_R^m+ik_z z_R^m][in\Delta k_x n_x+ik_z n_z]\}.\quad(15)$$

In equations 14 and 15, $V_{\vec{n}}$ is the measured normal particle velocity wavefield (particle velocity sensor is gimbled to measure the normal particle velocity wavefield), P is the measured pressure wavefield, ω is the angular frequency, ρ is the density, x_R^m is the horizontal position of the receiver m, z_R^m is the depth position of receiver m, Δk_x is the discretized horizontal wavenumber, n is a running index for the horizontal wavenumbers, k_z is the vertical wavenumber, n_x and n_z are, respectively the horizontal and vertical components of the normal vector to the receivers, Δx is the spacing between the receivers (here 12.5 m), P^{up} and P^{down}, respectively denote the decomposed upgoing and downgoing pressure wavefields.

Figure 9 shows a plot of the depth variation of the receivers for the first shot that is analyzed. Because the streamer depth variation is about 0.2 m around the nominal depth, the effect will be a small vertical displacement of the imaged sea surface as shown in Figure 7 using synthetic data if not accounted for. Figure 10a shows a field record of the total pressure wavefield at 15 m depth for shot 3000. After wavefield separation, the separated upgoing and downgoing wavefields were extrapolated to the sea surface where an adequate imaging condition was applied in a sliding window mode. As before, the imaging technique was applied within a 400 ms window but now the window is slid 100 ms each time to obtain time variable changes of the sea surface for a given receiver position. Figure 10b shows a surface plot of the imaged sea surface obtained by interpolating linearly between sea surface profiles imaged at different times. The holes seen at the earlier times of the plot are parts where no data were recorded while the holes seen at the later parts of the plot are where the recorded data show poor signal-to-noise ratio (S/N) as shown by the red inset in Figure 10a. The missing data at either ends of the plot result from truncation of the input data. The inset shown in black defines the area where the spectral analysis of the sea surface profiles for four consecutive shots of the field data will be carried out.

Figure 11 shows surface plots of the sea surface to be used in the spectral analysis of the four consecutive shots. Observe the good

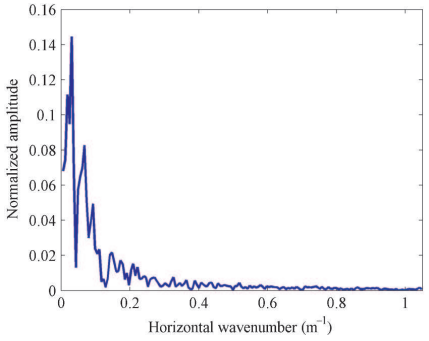

Figure 8. Averaged Pierson-Moskowitz spectrum based on a modeled sea surface with a prevailing wind speed of 17 m/s.

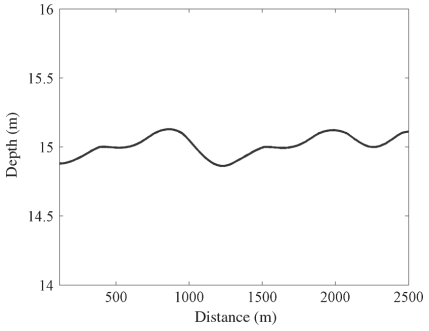

Figure 9. Interpolated plot of the streamer depth variation for shot 3000.

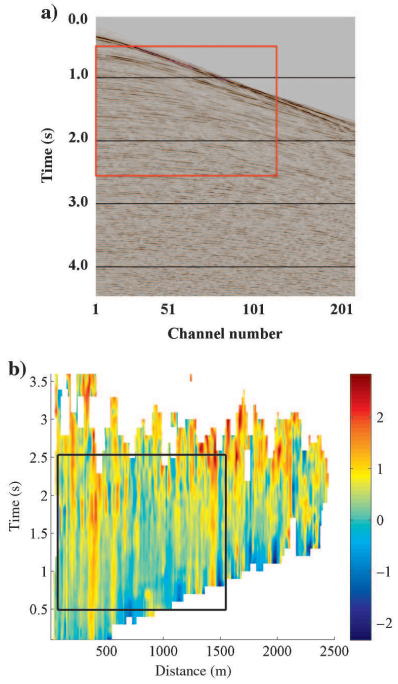

Figure 10. (a) Field record of the total pressure wavefield at 15 m depth for shot 3000. The red inset box marks the field record window where a reliable sea surface image was obtained (see the corresponding black inset box in Figure 10b). (b) Surface plot of the imaged sea surface from the same shot. The black box indicates also the part of the sea surface used in the spectral analysis.

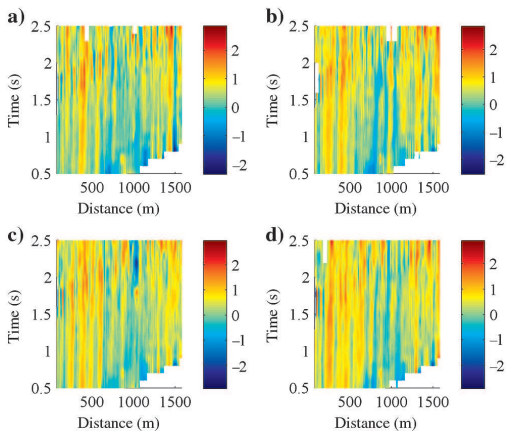

Figure 11. Surface plots of the imaged sea surfaces for four consecutive shots (a) shot 3000, (b) 3001, (c) 3002, and (d) 3003 covering the area defined by the box in Figure 10a and 10b.

correlation between the imaged sea surfaces from these shots. The overall pattern is the same and apparent sea surface wave speeds are similar in the four shots. In total, the part of the data that is imaged is about 4 s long whereas the part taken for the spectral analysis is 2.5 s. However, because the data length is about 10 s long which implies that the shot firing interval is about 12 s, the continuity in terms of the character of the time-varying sea-surface from one shot to another cannot be expected to be smooth in general. The imaging technique is dependent on the measured level of scattered upgoing and downgoing wavefields relative to the noise in the imaging window. Thus, if the S/N is enhanced at the lower part of the data, a smooth transition in the imaged sea surface from one shot to the other would be possible.

Spectral analysis of sea surface

The feasibility of carrying out a spectral analysis to estimate the dominating wave speed has already been demonstrated in case of a Pierson-Moskowitz sea surface condition. The same procedure is now applied to the imaged sea surfaces from the field data for the shots shown in Figure 11. By averaging the spectra within observation times between 0.8 and 2.5 s for each of the four shots, the results shown in Figure 12 were obtained. Note the good correlation among these averaged spectra. This is expected because these shots are consecutive and also because the averaged wave statistics are assumed to vary in a smooth manner. By considering the peak wavenumber value associated with each shot point, an average surface wave apparent speed of approximately 16.4 m/s was obtained. This estimate represents a realistic value (note that the values at very low wavenumbers represent end effects because of data truncation). However, given the limited number of profiles that are averaged, this estimated apparent sea surface wave speed may vary slightly if a larger number of profiles are considered.

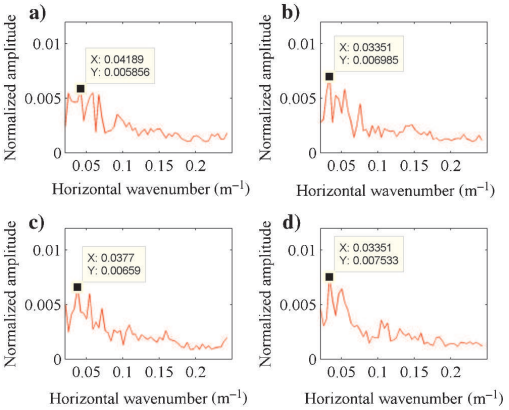

Figure 12. Plot of the average spectrum for the imaged sea profiles for four consecutive shots ((a) 3000, (b) 3001, (c) 3002, and (d) 3003) averaged between observation times 0.8–1.6 s. The peak values of the wavenumber are also indicated corresponding to a surface speed of about 16.4 m/s.

CONCLUSIONS

A method of modeling scattered wavefields from time-varying sea surfaces has been presented. This is based on the Kirchhoff-Helmholtz integral with the Kirchhoff approximation included and the accuracy was demonstrated by comparing it with the "exact solution" for a frozen sea surface case. Controlled scattering could now be generated for realistic time-varying sea surfaces. By extrapolating the scattered decomposed upgoing and downgoing wavefields toward the sea surface and applying an adequate imaging condition in a sliding window mode, the robustness of the concept of imaging time-varying sea surfaces was demonstrated.

In the limit of a typical seismic bandwidth (8–125 Hz) associated with an air gun array, the effect of a typical vessel speed (2.5 m/s) on the image of moderately rough sea surfaces (wind speed less than 20 m/s according to Beaufort scale) is negligible. For receivers moving at speeds higher than typical seismic vessel speeds, the effect is a lateral translation (in the direction of the seismic vessel) of the imaged sea surface. Nevertheless, the directional effects of time-varying sea surfaces are not included because we employed a 1D Pierson-Moskowitz roughness spectrum in the modeling. However, in case of a real seismic data acquisition, the movements of the sea surface are complicated; thus the effects of a moving sea surface and moving receivers are not restricted to simple lateral shifts of the imaged sea surface. Furthermore, imaging the sea surface without taking the true receiver depths into account resulted in sea surface images displaced vertically from the reference or nominal depth level. By accounting for variable streamer depth during the imaging process, these artifacts were removed.

Sea surface waves are dispersive with the group velocity representing the speed of the main energy (close to the wind speed). Using the Pierson-Moskowitz modeled sea surface at a fixed time as input to a spectral analysis and averaging over different observation times the peak wavenumber could be identified. In combination with the deep-water dispersion relation the corresponding surface wave velocity could be estimated. The same approach was tested on four consecutive shot points from a field data set from the North Sea, demonstrating the feasibility of estimating the surface wave velocity in a practical setting. These four shot points were also used to image the time-variant sea surface. High correlations were obtained between the images. However due to poor S/Ns in parts of the data, the final images were incomplete. To improve the S/N and reduce the area of missing data in the imaged sea surface, the concept of blended shooting could be used. Because the imaging technique relies only on the measured scattered events and their receiver ghosts, it is beneficial to have a large number of events in every imaging window. Additional knowledge of the active blended sources (e.g., positions and firing times) is not required. Parts of the sea surface with high frequency spatial roughness (i.e., short relative wavelengths and wave heights) are not sensed during data acquisition, and consequently not present in the imaging. This is due to the limited frequency bandwidth associated with a typical seismic air gun array. Thus, the time-varying sea surface obtained here is relatively smooth and can be considered as a filtered version of the true sea surface which has a broader spatial wavenumber spectrum.

This work has in a systematic manner addressed typical time-varying effects of the sea surface in marine seismic data based on controlled modeling and 2D field data. Further work with this method will include the generalization to 3D acquisition geometries. In addition, as opposed to the frequency-space domain currently used, the imaging condition could be rather applied in the frequency-wavenumber domain. This formulation is tailored for the estimation of angle-dependent sea-surface reflection coefficients. Estimation of such reflection coefficients based on statistical techniques will be a highly prioritized task in our future work.

ACKNOWLEDGMENTS

We thank PGS for permission to publish this work. Orji acknowledges funding from the Norwegian Research Foundation (NFR) through an industrial Ph.D. grant.

APPENDIX A

KIRCHHOFF-HELMHOLTZ INTEGRAL (FREQUENCY-DOMAIN)

The Kirchhoff-Helmholtz integral equation in the frequency-domain can be written as (e.g., Thorsos, 1988, 1990; Amundsen, 1994; Siderius and Porter, 2008):

$$P(\vec{r},\omega) = P_{inc}(\vec{r},\omega) - \frac{1}{4i}\int_{\partial L}[H_0^{(1)}(k|\vec{r}\,' - \vec{r}|)]\frac{\partial P(\vec{r}\,',\omega)}{\partial n'}dl', \quad \text{(A-1)}$$

where the first term represents the direct wavefield and the second term the scattered wavefield from the sea surface. $S(\omega)$ represents the source spectrum. When the surface is locally planar on the scale of the dominating acoustic wavelength, the Kirchhoff approximation can be used to approximate the pressure gradient:

$$\frac{\partial P(\vec{r},\omega)}{\partial n} \cong \frac{2\partial P_{inc}(\vec{r},\omega)}{\partial n}. \quad \text{(A-2)}$$

Equations A-1 and A-2 can be combined to give:

$$P(\vec{r},\omega) = \frac{S(\omega)}{4i}H_0^{(1)}(k|\vec{r}_d|) + \frac{1}{8}\int_{\partial L}[H_0^{(1)}(k|\vec{r}\,' - \vec{r}|)]\frac{\partial H_0^{(1)}(k|\vec{\rho}|)}{\partial n'}dl'. \quad \text{(A-3)}$$

The normal derivative in equation A-3 can be further elaborated as follows:

$$\frac{\partial H_0^{(1)}(k|\vec{\rho}|)}{\partial n'} = \frac{\partial H_0^{(1)}(k|\vec{\rho}|)}{\partial(k|\vec{\rho}|)}\hat{\rho}\cdot\hat{n}' = -H_1^{(1)}(k|\vec{\rho}|)\hat{\rho}\cdot\hat{n}'. \quad \text{(A-4)}$$

Substituting equation A-4 in equation A-3 gives:

$$P(\vec{r},\omega) = \frac{S(\omega)}{4i}H_0^{(1)}(k|\vec{r}_d|) - \frac{kS(\omega)}{8}\int_{\partial L}H_0^{(1)}(k|\vec{r}\,' - \vec{r}|)\, H_1^{(1)}(k|\vec{\rho}|)\hat{\rho}\cdot\hat{n}'dl', \quad \text{(A-5)}$$

where $\hat{\rho}\cdot\hat{n}'$ is the obliquity factor. From Figure (1) in the main text, it follows that the unit vector of the surface pressure gradient, $\hat{\rho}$, at the point $[x', f(x')]$ is given as:

$$\hat{\rho} = \frac{(x' - x_s)\hat{i}}{|\vec{\rho}|} + \frac{[f(x') - z_s]\hat{k}}{|\vec{\rho}|}. \quad \text{(A-6)}$$

Similarly, from Figure A-1 the unit vector, $\hat{n}$, denoting the normal to the surface at the running scattering point is given as:

$$\hat{n}' = \cos(\phi)\left[\left.\frac{df(x)}{dx}\right|_{x=x'}\hat{i} - \hat{k}\right], \quad \text{(A-7)}$$

with

$$\tan(\phi) = \left.\frac{df(x)}{dx}\right|_{x=x'}.$$

Combining equations A-6 and A-7 gives:

$$\hat{\rho}\cdot\hat{n}' = -\cos(\phi)\left(\frac{-(x' - x_s)\left.\frac{df(x)}{dx}\right|_{x=x'}}{|\vec{\rho}|} + \frac{[f(x') - z_s]}{|\vec{\rho}|}\right). \quad \text{(A-8)}$$

Furthermore, using the method of surface parameterization, an infinitesimally small element of the rough surface can be expressed as:

$$dl' = dx'\sqrt{1 + \left(\left.\frac{df(x)}{dx}\right|_{x=x'}\right)^2} = \gamma dx' = \frac{dx'}{|\cos(\phi)|}. \quad \text{(A-9)}$$

Finally, equations A-5, A-8, and A-9 are combined to give the frequency-domain Kirchhoff-Helmholtz integral:

$$P(\vec{r},\omega) = \frac{1}{4i}H_0^{(1)}(k|\vec{r}_d|)S(\omega) + \frac{kS(\omega)}{8}\int_{\partial L} H_0^{(1)}(k|\vec{r}' - \vec{r}|)H_1^{(1)}(k|\vec{\rho}|)\eta(x')dx', \quad \text{(A-10)}$$

with the obliquity factor given explicitly as:

$$\eta(x') = \frac{-(x' - x_s)\left.\frac{df(x)}{dx}\right|_{x=x'}}{|\vec{\rho}|} + \frac{[f(x') - z_s]}{|\vec{\rho}|}. \quad \text{(A-11)}$$

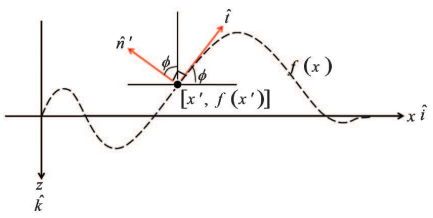

Figure A-1. A sketch showing the tangent and the normal to the rough surface at the running scattering point position.

APPENDIX B

KIRCHHOFF-HELMHOLTZ INTEGRAL (TIME-DOMAIN)

The asymptotic forms of the Hankel function of first kind are given as (e.g., Watson, 1962; Abramowitz and Stegun, 1972; Arfken, 1985):

$$H_n^{(1)}(x) \cong \sqrt{\frac{2}{\pi x}}e^{i\left(x - \frac{\pi}{4} - \frac{n\pi}{2}\right)}, \qquad n = 0, 1, 2, \ldots\ldots \quad \text{(B-1)}$$

With the use of B-1, the first term on the right-hand-side of equation A-10 representing the incident field can be rewritten as follows:

$$P_{inc}(\vec{r},\omega) = \frac{1}{2}\sqrt{\frac{c}{2\pi|\vec{r}_d|}}e^{-i\frac{3\pi}{4}}\frac{1}{\sqrt{\omega}}S(\omega)e^{i(\omega\tau_d)}, \quad \text{(B-2)}$$

with

$$\tau_d = \frac{|\vec{r}_d|}{c}.$$

After inverse Fourier transform, the time-domain version of the incident wavefield can be expressed as:

$$P(\vec{r},t) = \frac{1}{2}\sqrt{\frac{c}{2\pi|\vec{r}_d|}}q(t - \tau_d), \quad \text{(B-3)}$$

where q is a filtered version of the original pulse:

$$e^{-i\frac{3\pi}{4}}\frac{1}{\sqrt{\omega}}S(\omega) \overset{IFT}{\rightarrow} q(t).$$

Similarly, the scattered wavefield in the frequency-domain (e.g., second term on the right-hand-side of A-10) can be rewritten using equation B-1:

$$P_{scat}(\vec{r},\omega) = -\frac{S(\omega)}{4\pi}\int_{\partial L}\frac{1}{\sqrt{|\vec{r}' - \vec{r}||\vec{\rho}|}}e^{i\omega\left(\frac{|\vec{r}' - \vec{r}|}{c} + \frac{\vec{\rho}}{c}\right)}\eta(x')dx', \quad \text{(B-4)}$$

Applying an inverse Fourier transform gives the time-domain version of the scattered field:

$$P_{scat}(\vec{r},t) = -\frac{1}{4}\int_{\partial L}\frac{1}{\sqrt{|\vec{r}' - \vec{r}||\vec{\rho}|}}s(t - \tau(x'))\eta(x')dx', \quad \text{(B-5)}$$

with

$$\tau = \tau_s + \tau_r = \frac{|\vec{\rho}|}{c} + \frac{|\vec{r}' - \vec{r}|}{c}.$$

Combining equations B-2 and B-5 gives the time-domain Kirchhoff-Helmholtz solution.

REFERENCES

Abramowitz, M., and I. A. Stegun, 1972, Handbook of mathematical functions with formulas, graphs and mathematical tables: 9th printing: Dover.

Alpers, W., 1983, Monte Carlo simulations for studying the relationship between ocean wave and synthetic aperture radar image spectra: Journal of Geophysical Research, **88**, no. C3, 1745–1759, doi: 10.1029/JC088iC03p01745.

Amundsen, L., 1993, Wave-number-based filtering of marine point source data: Geophysics: **58**, 1335–1348, doi: 10.1190/1.1443516.

Amundsen, L., 1994, The propagator matrix related to the Kirchhoff-Helmholtz integral in inverse wavefield extrapolation: Geophysics, **59**, 1902–1910, doi: 10.1190/1.1443577.

Arfken, G., 1985, Mathematical methods for physicists, 3rd ed.: Academic Press.

Carlson, D., A. Long, W. Söllner, H. Tabti, R. Tenghamn, and N. Lunde, 2007, Increased resolution and penetration from a towed dual-sensor streamer: First Break, **25**, 71–77.

Claerbout, J. F., 1971, Toward a unified theory of reflector mapping: Geophysics, **36**, 467–481, doi: 10.1190/1.1440185.

Claerbout, J. F., 1976, Fundamentals of geophysical data processing: McGraw-Hill.

Clay, C. S., and H. Medwin, 1977, Acoustical oceanography: Principles and applications: John Wiley and Sons.

Fokkema, J. T., and P. M. van den Berg, 1993, Seismic applications of acoustic reciprocity: Elsevier Science Publishers.

Hasselmann, K., and S. Hasselmann, 1991, On the nonlinear mapping of an ocean wave spectrum into a synthetic aperture radar image spectrum: Journal of Geophysical Research, **96**, no. C6, 10713–10729, doi: 10.1029/91JC00302.

Holford, R. L., 1981, Scattering of sound waves at a periodic, pressure-release surface: An exact solution: Journal of the Acoustical Society of America, **70**, no. 4, 1116–1128, doi: 10.1121/1.386943.

Ishimaru, A., 1997, Wave propagation and scattering in random media: Oxford University Press.

Laws, R., and E. Kragh, 2002, Rough seas and time-lapse seismic: Geophysical Prospecting, **50**, 195–208, doi: 10.1046/j.1365-2478.2002.00311.x.

Meecham, W. C., 1956, On the use of the Kirchhoff approximation for the solution of reflection problems: Journal of Rational Mechanics Analysis, **5**, 323–334.

Neumann, G., and W. J. Pierson, 1966, Principles of physical oceanography: Prentice-Hall.

Orji, O., W. Söllner, and L. J. Gelius, 2010, Imaging the sea surface using a dual-sensor towed streamer: Geophysics, **75**, no. 6, V111–V118, doi: 10.1190/1.3496439.

Pierson, W. J., and L. Moskowitz, 1964, A proposed spectral form for fully-developed wind seas based on the similarity theory of A. A. Kitaigorodskii: Journal of Geophysical Research, **69**, 5181–5190, doi: 10.1029/JZ069i024p05181.

Pond, S., and G. L. Pickard, 1983, Introduction to dynamical oceanography: 2nd ed., Butterworth-Heinemann Ltd.

Schleicher, J., J. Costa, and A. Novais, 2008, A comparison of imaging conditions for wave-equation shot-profile migration: Geophysics, **73**, no. 6, S219–S227, doi: 10.1190/1.2976776.

Schneider, A. W., K. L. Larner, J. P. Burg, and M. M. Backus, 1964, A newdata-processing technique for the elimination of ghost arrivals on reflection seismograms: Geophysics, **29**, 783–805, doi: 10.1190/1.1439419.

Schulz-Stellenfleth, J., J. Horsmann, S. Lehner, and W. Rosenthal, 2001, Sea surface imaging with an across-track interferometric sythetic aperture radar: The SINEWAVE experiment: IEEE Transactions on Geoscience and Remote Sensing, **39**, no. 9, 2017–2028, doi: 10.1109/36.951092.

Schulz-Stellenfleth, J., and S. Lehner, 2001, Ocean wave imaging using an airborne single pass cross track interferometric SAR: IEEE Transactions on Geoscience and Remote Sensing, **39**, no. 1, 38–44, doi: 10.1109/36.898663.

Siderius, M., and M. B. Porter, 2008, Modeling broadband ocean acoustic transmissions with time-varying sea surface: Journal of the Acoustical Society of America, **124**, no. 1, 137, doi: 10.1121/1.2920959.

Söllner, W., A. Day, and H. Tabti, 2008, Space-frequency domain processing of irregular dual-sensor streamer data: 78th Annual International Meeting, SEG, Expanded Abstracts, 1078–1082.

Stojanovic, M., 1996, Recent advances in high-speed underwater acoustic communications: IEEE Journal of Oceanic Engineering, **21**, no. 2, 125–136, doi: 10.1109/48.486787.

Tenghamn, R., S. Vaage, and C. Borresen, 2007, A dual-sensor, towed marine streamer; its viable implementation and initial results: 77th Annual International Meeting, SEG, Expanded Abstracts, 989–993.

Thorsos, E. I., 1988, The validity of the Kirchhoff approximation for rough surface scattering using a Gaussian roughness spectrum: Journal of the Acoustical Society of America, **83**, no. 1, 78–92, doi: 10.1121/1.396188.

Thorsos, E. I., 1990, Acoustic scattering from a "Pierson-Moskowitz" sea surface: Journal of the Acoustical Society of America, **88**, no. S1, 335, doi: 10.1121/1.399909.

Urick, R. J., 1983, Principles of underwater sound: Mcgraw-Hill Book Company.

Watson, G. N., 1962, A treatise on the theory of Bessel functions: Syndics of the Cambridge University Press.

Paper III

2D time-varying sea surface imaging using 3D towed dual-sensor streamers

Orji O. C., W. Söllner and L-J. Gelius

Geophysics (Revised version submitted July 2012)